Nonlinear optical Hall effect of few-layered $NbSe_2$

Ren Habara [1] and Katsunori Wakabayashi [1,2,3]

[1] Department of Nanotechnology for Sustainable Energy, School of Science and Technology, Kwansei Gakuin University, Gakuen 2-1, Sanda 669-1337, Japan

[2] National Institute for Materials Science (NIMS), Namiki 1-1, Tsukuba 305-0044, Japan

[3] Center for Spintronics Research Network (CSRN), Osaka University, Toyonaka 560-8531, Japan

(Received 27 December 2021; revised 14 February 2022; accepted 8 March 2022; published 23 March 2022)

$NbSe_2$ is one of metallic two-dimensional (2D) transition-metal dichalcogenide (TMDC) materials. Because of broken crystal inversion symmetry, large spin splitting is induced by Ising-type spin-orbit coupling in odd-number-layered $NbSe_2$, but absent for even-number-layered $NbSe_2$ with the inversion symmetry. In this paper we numerically calculate nonlinear optical charge and spin Hall conductivities of few-layered $NbSe_2$ based on an effective tight-binding model which includes d_{z^2}, $d_{x^2-y^2}$, and d_{xy} orbitals of Nb atoms. We show that the nonlinear optical Hall conductivity for the second harmonic generation (SHG) process has a nonvanishing value in odd-number-layered $NbSe_2$. Also, we provide a nonlinear optical selection rule in few-layered $NbSe_2$ and their polarization dependencies. Furthermore, for the even-number-layered case, the nonlinear optical Hall currents can be generated by applying electric fields which break inversion symmetry. We also discuss that the nonlinear optical Hall effect is expected to occur in TMDC materials in general. Thus, our results will serve to design potential opt-spintronics devices based on 2D materials to generate the spin Hall current by SHG.

DOI: 10.1103/PhysRevResearch.4.013219

I. INTRODUCTION

Transition metal dichalcogenide (TMDC) with a chemical formula MX_2 (M = Mo, W, Nb, Ta; X = S, Se) is a new class of two-dimensional (2D) electronic systems, which provides the platform to design functional opt-electronic devices [1–9]. Owing to weak van der Waals forces between layers, bulk TMDC can be easily exfoliated into monolayer [10–14]. In monolayer MoS_2 and WSe_2, the valley-dependent optical excitation [15–18] and intrinsic spin Hall effect (SHE) [19–22] have been reported. Furthermore, nonlinear optical effect such as second-harmonic generation (SHG) [23–35], sum-frequency generation (SFG) [36–42], third-harmonic generation (THG) [23,43–45], high-harmonic generation (HHG) [23,46–48], and two-photon absorption [23,49–51] has been extensively studied. In general, the nonlinear optical effect is sensitive to crystal symmetries and phase-matching conditions between an incident light and a light-induced electric polarization wave. However, the phase-matching conditions are not necessary for nonlinear optical effect in atomically thin 2D materials, because their thickness is much smaller than the light wavelength [23,52,53]. Thus, in atomically thin 2D materials such as TMDCs, the nonlinear optical effect strongly depends on the crystal symmetry. In addition, it has been recently discussed that second order anomalous transport phenomena in the absence of magnetic field can be induced by uniaxial strain in metallic TMDC, i.e., nonlinear Hall effect, which has a relation with a Berry curvature dipole [54–57].

$NbSe_2$ is metallic TMDC which shows superconducting phase transition at low temperatures [58–64]. In this material, AB-stacking structure is most stable in nature and has different crystal symmetries for even and odd number of layers. In even-number-layered $NbSe_2$, the crystal structure has a space group D_{3d}, which respects inversion and out-of-plane mirror symmetries. On the other hand, odd-number-layered $NbSe_2$ has a space group D_{3h}, which possesses out-of-plane mirror symmetry, but no spacial inversion symmetry. Because of the broken inversion symmetry and a strong spin-orbit coupling (SOC) field of Nb atoms in odd-number-layered $NbSe_2$, it possesses Ising-type SOC [60–62,65–68], i.e., an effective Zeeman field that locks electron spins to out-of-plane directions by in-plane momentum and causes larger spin splitting in the energy band structures leading to unconventional topological spin properties. Actually we have analyzed the linear optical properties of monolayer $NbSe_2$ using Kubo formula based on an effective tight-binding model (TBM) and shown that the spin Hall current can be induced by irradiating visible light owing to its finite spin Berry curvature [69].

In this paper we extend our theoretical analysis to nonlinear optical spin and charge Hall conductivities of SHG process for few-layered $NbSe_2$. Here we have employed the effective TBM to describe the electronic structures of few-layered $NbSe_2$, where the electron hoppings among d_{z^2}, $d_{x^2-y^2}$, and d_{xy} orbitals of Nb atom and Ising-type SOC are included. Numerical calculation shows that owing to the

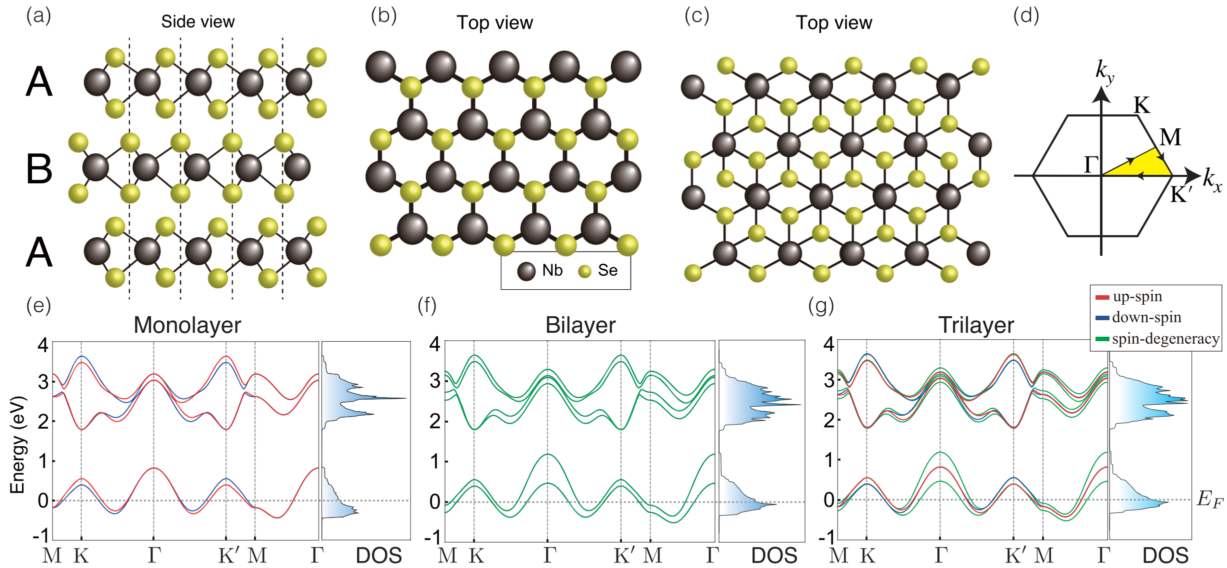

FIG. 1. Crystal structures of different few-layered $NbSe_2$ which consist of Nb (black) and Se (yellow) atoms. (a) Side view of the lattice structure of monolayer (A), bilayer (AB), and trilayer (ABA) $NbSe_2$. Top views of the lattice structures of (b) monolayer and (c) bilayer and trilayer $NbSe_2$. (d) First BZ of $NbSe_2$. Energy band structures and DOS of (e) monolayer, (f) bilayer, and (g) trilayer $NbSe_2$ with SOC parameter $\lambda_{SOC} = 0.0784$ eV, respectively. Fermi level is set to zero.

broken inversion symmetry, the nonlinear optical Hall currents are generated in odd-number-layered $NbSe_2$, but absent for even-number-layered $NbSe_2$. In particular, under irradiating y-polarized visible light, nonlinear spin Hall current appears. On the other hand, the x-polarized visible light generates a nonlinear charge Hall current. Furthermore, for even-number-layered $NbSe_2$, the spin and charge Hall current can be generated if the out-of-plane mirror and inversion symmetries are broken by the application of electric fields perpendicular to the plane. Thus, we provide a nonlinear optical selection rule of spin and charge Hall currents in few-layered $NbSe_2$, which clarifies the even-odd effect of layer numbers and light polarization dependencies. Our results will serve to design potential opt-spintronics devices on the basis of 2D materials.

This paper is organized as follows. In Sec. II we discuss the effective model of even- and odd-number-layered $NbSe_2$ which includes crystal structure and energy band structure. In Sec. III we numerically calculate nonlinear optical spin and charge Hall conductivities for alternating current (AC) fields and find that the nonlinear optical Hall currents strongly depend on layer numbers and polarization of incident light. In Sec. IV we discuss that when the crystal symmetry is broken by applying electric fields, nonlinear optical Hall currents can be generated even in even-number-layered $NbSe_2$. In Sec. V we summarize our results. In addition, in the Appendixes we show details of matrix elements in an effective Hamiltonian. Also, we present contour plots of integrands for nonlinear optical spin and charge Hall conductivities and energy band structures of bilayer $NbSe_2$ with the application of electric fields. In the Supplemental Material we provide the details of the second order nonlinear optical conductivities, temperature effect for odd-number-layered $NbSe_2$, and nonlinear optical Hall conductivity of monolayer MoS_2 as a reference example of a TMDC semiconductor [70].

II. MODEL

In this paper we show that nonlinear optical spin and charge currents of few-layered $NbSe_2$ strongly depend on the crystal symmetry and number of stacking layers. Especially, we focus on the cases of monolayer, AB-stacked bilayer, and ABA-stacked trilayer $NbSe_2$. Figure 1(a) shows schematic of few-layered $NbSe_2$ with AB stacking, which is the most energetically stable stacking sequence in $NbSe_2$. Each layer has the out-of-plane mirror symmetry with respect to the plane of Nb atoms. Figures 1(b) and 1(c) show the top views of monolayer $NbSe_2$ and AB-stacked few-layered $NbSe_2$, respectively. In the even-number-layered case, $NbSe_2$ has a space group D_{3d}, which respects inversion symmetry. However, in the case of odd-number-layered $NbSe_2$, it has a space group D_{3h}, which has no spatial inversion symmetry. Figure 1(d) shows the first Brillouin zone (BZ) for few-layered $NbSe_2$.

We employ a multiorbitals TBM which includes d_{z^2}, $d_{x^2-y^2}$, and d_{xy} orbitals of Nb atom to describe the electronic states of $NbSe_2$ [60,69,71]. The eigenvalue equation for TBM is $\hat{H}(\boldsymbol{k})|u_{n\boldsymbol{k}}\rangle = E_{n\boldsymbol{k}}|u_{n\boldsymbol{k}}\rangle$, where $\boldsymbol{k} = (k_x, k_y)$ is the wave-number vector, $E_{n\boldsymbol{k}}$ is the eigenvalue, and $n = 1, 2, \dots, 6N$ (N is the number of layers) is the band index. The eigenvector is defined as $|u_{n\boldsymbol{k}}\rangle = (c_{n\boldsymbol{k},\, d_{z^2},\uparrow},\ c_{n\boldsymbol{k},d_{xy},\uparrow},\ c_{n\boldsymbol{k},d_{x^2-y^2},\uparrow}, c_{n\boldsymbol{k},d_{z^2},\downarrow}, c_{n\boldsymbol{k},d_{xy},\downarrow}, c_{n\boldsymbol{k},d_{x^2-y^2},\downarrow})^T$, where $(\cdots)^T$ indicates the transpose of vector and $c_{n\boldsymbol{k}\tau s}$ means the amplitude at atomic orbital τ with spin s for the nth energy band at $\boldsymbol{k}$. The Hamiltonian of monolayer $NbSe_2$ with the SOC can be written as

$$\hat{H}_{\mathrm{mono}}(\boldsymbol{k}) = \hat{\sigma}_0 \otimes \hat{H}_{\mathrm{TNN}}(\boldsymbol{k}) + \hat{\sigma}_z \otimes \tfrac{1}{2}\lambda_{\mathrm{SOC}}\hat{L}_z, \tag{1}$$

with

$$\hat{H}_{\mathrm{TNN}}(\boldsymbol{k}) = \begin{pmatrix} V_0 & V_1 & V_2 \\ V_1^* & V_{11} & V_{12} \\ V_2^* & V_{12}^* & V_{22} \end{pmatrix} \tag{2}$$

and

$$\hat{L}_z = \begin{pmatrix} 0 & 0 & 0 \\ 0 & 0 & -2i \\ 0 & 2i & 0 \end{pmatrix}. \quad (3)$$

Here $\hat{\sigma}_0$ and $\hat{\sigma}_z$ are Pauli matrices and λ_{SOC} is the Ising-type SOC parameter. In monolayer $\mathrm{NbSe_2}$, $\lambda_{\mathrm{SOC}} = 0.0784\,\mathrm{eV}$. $\hat{H}_{\mathrm{TNN}}(\boldsymbol{k})$ includes the electron hoppings only among three d orbitals of Nb atoms, which are assumed up to third-nearest neighbor sites as shown in Appendix A. Similarly, Hamiltonians of bilayer and trilayer $\mathrm{NbSe_2}$ can be obtained as

$$\hat{H}_{\mathrm{bi}}(\boldsymbol{k}) = \begin{pmatrix} \hat{H}_{\mathrm{mono}}(-\boldsymbol{k}) & \hat{H}_{\mathrm{int}}(\boldsymbol{k}) \\ \hat{H}^{\dagger}_{\mathrm{int}}(\boldsymbol{k}) & \hat{H}_{\mathrm{mono}}(\boldsymbol{k}) \end{pmatrix} \quad (4)$$

and

$$\hat{H}_{\mathrm{tri}}(\boldsymbol{k}) = \begin{pmatrix} \hat{H}_{\mathrm{mono}}(\boldsymbol{k}) & \hat{H}_{\mathrm{int}}(\boldsymbol{k}) & 0 \\ \hat{H}^{\dagger}_{\mathrm{int}}(\boldsymbol{k}) & \hat{H}_{\mathrm{mono}}(-\boldsymbol{k}) & \hat{H}_{\mathrm{int}}(\boldsymbol{k}) \\ 0 & \hat{H}^{\dagger}_{\mathrm{int}}(\boldsymbol{k}) & \hat{H}_{\mathrm{mono}}(\boldsymbol{k}) \end{pmatrix}, \quad (5)$$

respectively [62]. Here interlayer coupling Hamiltonian $\hat{H}_{\mathrm{int}}(\boldsymbol{k})$ is considered as

$$\hat{H}_{\mathrm{int}}(\boldsymbol{k}) = \begin{pmatrix} T_{01} & 0 & 0 \\ 0 & T_{02} & 0 \\ 0 & 0 & T_{02} \end{pmatrix}. \quad (6)$$

The details of matrix elements V_0, V_1, V_2, V_{11}, V_{12}, V_{22}, T_{01}, and T_{02} can be found in Appendix A.

Figures 1(e)–1(g) show the energy band structures of monolayer, bilayer, and trilayer $\mathrm{NbSe_2}$ together with the corresponding density of states (DOS), respectively. Here, red, blue, and green lines indicate spin-up, spin-down, and spin-degenerated states. $\mathrm{NbSe_2}$ is metallic, but there is a large energy band gap between the partially filled valence bands and empty conduction bands. Also, opposite spin splitting in the energy band structure can be seen at the valence band edges in K and K' points in monolayer $\mathrm{NbSe_2}$ owing to the broken inversion symmetry. However, because even-number-layered $\mathrm{NbSe_2}$ such as bilayer respect the inversion symmetry, it does not show the spin splitting. It should be noted that even-number-layered $\mathrm{NbSe_2}$ has larger band splitting at valence band in Γ point, because the interlayer interaction becomes larger in Γ point than in K and K' points. Figure 1(g) shows the calculated energy band structure of trilayer $\mathrm{NbSe_2}$, which can be understood by overwriting spin degenerated energy band structure of bilayer $\mathrm{NbSe_2}$ onto that of spin-splitting energy dispersion of monolayer $\mathrm{NbSe_2}$. Since the inversion symmetry is broken in odd-number-layered $\mathrm{NbSe_2}$, spin degeneracy is lifted. However, owing to the existence of spin degenerated energy band of bilayer $\mathrm{NbSe_2}$, the spin splitting at K and K' points is not clearly seen. The details of Fermi spin-dependent surface structures are shown in Appendix A.

III. NONLINEAR OPTICAL HALL CONDUCTIVITY

We numerically calculate nonlinear optical spin and charge Hall conductivities for few-layered $\mathrm{NbSe_2}$ based on an effective TBM. In general, the second order nonlinear optical spin conductivity can be given as [28,29,33,35,72–77]

$$\sigma^{\mathrm{spin}}_{ijk}(\omega_1,\omega_2) \equiv -\frac{\hbar^2 e^2}{S}\sum_{\boldsymbol{k}} \Omega^{\mathrm{spin}}_{ijk}(\omega_1,\omega_2,\boldsymbol{k}), \quad (7)$$

with

$$\begin{aligned}\Omega^{\mathrm{spin}}_{ijk}&(\omega_1,\omega_2,\boldsymbol{k})\\ &= \sum_{nml} \frac{1}{E_{ml}E_{ln}(E_{mn}-\hbar\omega_1-\hbar\omega_2-i\eta)}\\ &\times\Bigg[\frac{\langle u_{n\boldsymbol{k}}|\hat{v}_j|u_{l\boldsymbol{k}}\rangle\langle u_{l\boldsymbol{k}}|\hat{v}_k|u_{m\boldsymbol{k}}\rangle\langle u_{m\boldsymbol{k}}|\hat{j}^{\mathrm{spin}}_i|u_{n\boldsymbol{k}}\rangle f_{ml}}{E_{ml}-\hbar\omega_2-i\eta}\\ &-\frac{\langle u_{n\boldsymbol{k}}|\hat{v}_k|u_{l\boldsymbol{k}}\rangle\langle u_{l\boldsymbol{k}}|\hat{v}_j|u_{m\boldsymbol{k}}\rangle\langle u_{m\boldsymbol{k}}|\hat{j}^{\mathrm{spin}}_i|u_{n\boldsymbol{k}}\rangle f_{ln}}{E_{ln}-\hbar\omega_2-i\eta}\Bigg], \quad (8)\end{aligned}$$

where $\Omega^{\mathrm{spin}}_{ijk}(\omega_1,\omega_2,\boldsymbol{k})$ is an integrand of nonlinear optical spin conductivity. Here $i(j,k)$ indicates the direction x or y. In particular, i is the generation direction of nonlinear optical spin current, and $j(k)$ is the polarization of incident light. Also, $n(m,l)$ is the band index including spin degree of freedom, $|u_{n\boldsymbol{k}}\rangle$ is the eigenfunction with the eigenenergy $E_{n\boldsymbol{k}}$, and $f(E_{n\boldsymbol{k}})$ is the Fermi-Dirac distribution function. $E_{ml} \equiv E_m - E_l$, $f_{ml} \equiv f(E_{m\boldsymbol{k}}) - f(E_{l\boldsymbol{k}})$, and ω_q means the qth frequency mode. η is an infinitesimally small real number and S is the area of the system. Moreover, $\hat{j}^{\mathrm{spin}}_i$ is the spin current operator and written as $\hat{j}^{\mathrm{spin}}_i = \frac{1}{2}\{\frac{\hbar}{2}\hat{\sigma}_z\otimes\hat{I}_N,\hat{v}_i\}$, where $\hat{I}_N$ is the $N\times N$ identity matrix and $N = 3, 6, 9$ is used for monolayer, bilayer, and trilayer $\mathrm{NbSe_2}$, respectively. Here $\hat{v}_i = \frac{1}{\hbar}\frac{\partial\hat{H}}{\partial i}$ is the group velocity operator. The nonlinear optical charge conductivity $\sigma^{\mathrm{charge}}_{ijk}(\omega_1,\omega_2)$ is also obtained by changing $\hat{j}^{\mathrm{spin}}_i$ to $\hat{j}^{\mathrm{charge}}_i$ which is defined as $\hat{j}^{\mathrm{charge}}_i = \frac{1}{2}\{-e\hat{\sigma}_0\otimes\hat{I}_N,\hat{v}_i\}$. We add the superscript "spin" for the nonlinear optical spin conductivity in order to distinguish its conductivity from the nonlinear optical charge conductivity. In the case of $\omega_1+\omega_2=\omega_3$, the process is called as SFG (see Fig. S3) [70]. Especially in the case of $\omega_1=\omega_2\equiv\omega$, the process is called SHG. Also, in the case of $\omega_1-\omega_2=\omega_3$, the process is called difference frequency generation (DFG) [78,79]. Since we have interest in SHG, we focus on the SHG process in this paper, i.e., $\omega_1=\omega_2=\omega$.

The second order nonlinear optical conductivity expressed by Eq. (7) can be separated into two interband processes: (i) optical transition between two bands $\sigma^{(2)}_{ijk}$ and (ii) optical transition involving three bands $\sigma^{(3)}_{ijk}$ [76,80]. Namely, σ_{ijk} can be decomposed into

$$\sigma_{ijk}(\omega_1,\omega_2) = \sigma^{(2)}_{ijk}(\omega_1,\omega_2)+\sigma^{(3)}_{ijk}(\omega_1,\omega_2). \quad (9)$$

The detail of derivation can be found in Appendix B. In particular, considering the interband transition between two bands around Fermi surface, $\sigma^{(2)}_{ijk}$ can be rewritten as

$$\sigma^{(2)}_{ijk}(\omega_1,\omega_2\to 0) = -\frac{ie^2}{S}\frac{1}{\hbar\omega_1+i\eta}D_i, \quad (10)$$

where D_i is the Berry curvature dipole [57,81]

$$D_i = \sum_{\boldsymbol{k}}\sum_n \Omega_n(\boldsymbol{k})\,\langle u_{n\boldsymbol{k}}|\hat{j}_i|u_{n\boldsymbol{k}}\rangle\,\frac{\partial f_{n\boldsymbol{k}}}{\partial E_{n\boldsymbol{k}}}. \quad (11)$$

TABLE I. Nonlinear optical spin and charge conductivities of mono, bi, and trilayer $NbSe_2$. The conductivities of monolayer $NbSe_2$ are summarized in Fig. S2.

	Nonlinear optical spin conductivity	Nonlinear optical charge conductivity
mono (D_{3h})	$\sigma^{\text{spin}}_{xxx}(\omega,\omega) = -\sigma^{\text{spin}}_{xyy}(\omega,\omega)$ $= -\sigma^{\text{spin}}_{yxy}(\omega,\omega) = -\sigma^{\text{spin}}_{yyx}(\omega,\omega)$	$\sigma^{\text{charge}}_{yyy}(\omega,\omega) = -\sigma^{\text{charge}}_{yxx}(\omega,\omega)$ $= -\sigma^{\text{charge}}_{xyx}(\omega,\omega) = -\sigma^{\text{charge}}_{xxy}(\omega,\omega)$
bi (D_{3d})	zero	zero
tri (D_{3h})	$\sigma^{\text{spin}}_{xxx}(\omega,\omega) = -\sigma^{\text{spin}}_{xyy}(\omega,\omega)$ $= -\sigma^{\text{spin}}_{yxy}(\omega,\omega) = -\sigma^{\text{spin}}_{yyx}(\omega,\omega)$	$\sigma^{\text{charge}}_{yyy}(\omega,\omega) = -\sigma^{\text{charge}}_{yxx}(\omega,\omega)$ $= -\sigma^{\text{charge}}_{xyx}(\omega,\omega) = -\sigma^{\text{charge}}_{xxy}(\omega,\omega)$

Thus, the two-band process is nothing more than the effect of Berry curvature dipole. In the direct current (DC) limit, i.e., $\omega_1 \to 0$, D_i is identically zero in $NbSe_2$. However, it is expected to be finite even in the DC limit, if the uniaxial strain is applied to the system [57,81]. In this work we consider σ_{ijk} regardless of two-bands and three-bands interband processes.

Since the nonlinear optical conductivity σ_{ijk} is the third rank tensor, in general $\sigma^{\text{spin}}_{ijk}$ and $\sigma^{\text{charge}}_{ijk}$ have the $3^3 = 27$ components, respectively. However, using the Neumann's principle [23,24], we can find the nonvanishing elements of $\sigma^{\text{spin}}_{ijk}$ and $\sigma^{\text{charge}}_{ijk}$ from the crystal symmetry. Because the inversion symmetry is broken in monolayer $NbSe_2$, the nonvanishing tensor elements are obtained as following:

$$\sigma^{\text{spin}}_{xxx}(\omega,\omega) = -\sigma^{\text{spin}}_{xyy}(\omega,\omega) = -\sigma^{\text{spin}}_{yxy}(\omega,\omega) = -\sigma^{\text{spin}}_{yyx}(\omega,\omega) \tag{12}$$

and

$$\sigma^{\text{charge}}_{yyy}(\omega,\omega) = -\sigma^{\text{charge}}_{yxx}(\omega,\omega) = -\sigma^{\text{charge}}_{xyx}(\omega,\omega) = -\sigma^{\text{charge}}_{xxy}(\omega,\omega). \tag{13}$$

However, owing to the inversion symmetry in even-number-layered $NbSe_2$ such as bilayer $NbSe_2$, the nonlinear optical conductivities are obviously absent, i.e., all the tensor elements are identically zero. Also, since the crystal symmetry of trilayer $NbSe_2$ is identical to the monolayer $NbSe_2$, same relations of the nonlinear optical spin and charge conductivities are obtained using Neumann's principle. Table I summarizes the relations of nonvanishing tensor elements of $\sigma^{\text{spin}}_{ijk}$ and $\sigma^{\text{charge}}_{ijk}$ for few-layered $NbSe_2$. It should be noted that the nonlinear optical charge conductivity is zero, whenever the nonlinear optical spin conductivity has finite value. Since the second order nonlinear optical conductivity σ_{ijk} is a complex function of ω, the conductivity can be separated as

$$\sigma_{ijk}(\omega,\omega) = \text{Re}[\sigma_{ijk}(\omega,\omega)] + i\text{Im}[\sigma_{ijk}(\omega,\omega)], \tag{14}$$

where $\text{Re}[\sigma_{ijk}(\omega,\omega)]$ and $\text{Im}[\sigma_{ijk}(\omega,\omega)]$ are real and imaginary parts, respectively. In the main text we focus on the real part of σ_{ijk}. The details of the imaginary part of σ_{ijk} are shown in the Supplemental Material [70].

Figures 2(a)–2(c) show the real parts of nonlinear optical spin Hall conductivities $\text{Re}[\sigma^{\text{spin}}_{xyy}(\omega,\omega)]$ of monolayer, bilayer, and trilayer $NbSe_2$, respectively. Here $\text{Re}[\sigma^{\text{spin}}_{xyy}(\omega,\omega)]$ is considered as the case of SHG process and has Ising-type SOC parameter $\lambda_{\text{SOC}} = 0.0784$ eV. Also, the cases for $\lambda_{\text{SOC}} = 0.0392$ and 0 eV are plotted for the comparison. $\text{Re}[\sigma^{\text{spin}}_{xyy}(\omega,\omega)]$ represents that the spin Hall current is generated in x direction by irradiating y-polarized light. It mainly has two peaks around 1.5 and 2.5 eV for odd-number-layered $NbSe_2$ owing to even parity with respect to k_x and k_y axes in contour plot of $\Omega^{\text{spin}}_{xyy}(\omega,\omega,\boldsymbol{k})$ (see Appendix C). One peak can be seen around 1.5 eV, and indicates an excitation from valence band to conduction band by one incident photon at $2\hbar\omega$. The other peak around 2.5 eV shows that two incident photons at $\hbar\omega$ occurs an excitation from valence band to intermediate band and then conduction band.

Figures 2(d)–2(f) show the real parts of nonlinear optical charge Hall conductivities $\text{Re}[\sigma^{\text{charge}}_{yxx}(\omega,\omega)]$ of SHG process for monolayer, bilayer, and trilayer $NbSe_2$, respectively. $\text{Re}[\sigma^{\text{charge}}_{yxx}(\omega,\omega)]$ represents that the charge Hall current is generated in y direction by irradiating x-polarized light. There are mainly two peaks around 1.5 and 2.5 eV the same as the case of $\text{Re}[\sigma^{\text{spin}}_{xyy}(\omega,\omega)]$, which appear for $\text{Re}[\sigma^{\text{charge}}_{yxx}(\omega,\omega)]$ owing to the asymmetry of $\Omega^{\text{charge}}_{yxx}(\omega,\omega,\boldsymbol{k})$ with respect to k_x axis in contour plot (see Appendix C). For one incident photon at $2\hbar\omega$, one peak appears around 1.5 eV, and it is larger than the other peak around 2.5 eV which can be seen by two incident photons at $\hbar\omega$.

Thus, we can find that the nonlinear optical spin and charge Hall currents strongly depend on layer numbers and polarization of incident light in visible range, i.e., nonlinear optical selection rule of spin and charge Hall currents in few-layered $NbSe_2$.

Here we briefly mention the extreme similarity of the nonlinear optical conductivities between monolayer and trilayer $NbSe_2$ as shown in Fig. 2. The trilayer $NbSe_2$ can be viewed as the composite of monolayer and bilayer $NbSe_2$. Therefore, we have three contributions of optical transition processes: (A) intralayer optical transition of monolayer $NbSe_2$, (B) intra- and interlayer optical transition of bilayer $NbSe_2$, and (C) interlayer optical transitions between monolayer and bilayer $NbSe_2$. Since process (B) is identically zero, process (A) dominates the optical conductivities of trilayer $NbSe_2$. It is shown that process (C) is canceled because of band inversion along the Γ-K and Γ-K' lines in BZ. The detail can be found in the Supplemental Material [70].

Also, we have mentioned that the nonlinear optical Hall conductivity has the peaks (around 1.5 and 2.5 eV) corresponding to absorption of two photons in odd-number-layered $NbSe_2$, which cannot be seen for linearly optical Hall conductivity obtained by Kubo formula [69,82]. It should be noted that the magnitude of peak clearly corresponds to DOS of $NbSe_2$. The details of these peaks are shown in the Supplemental Material [70].

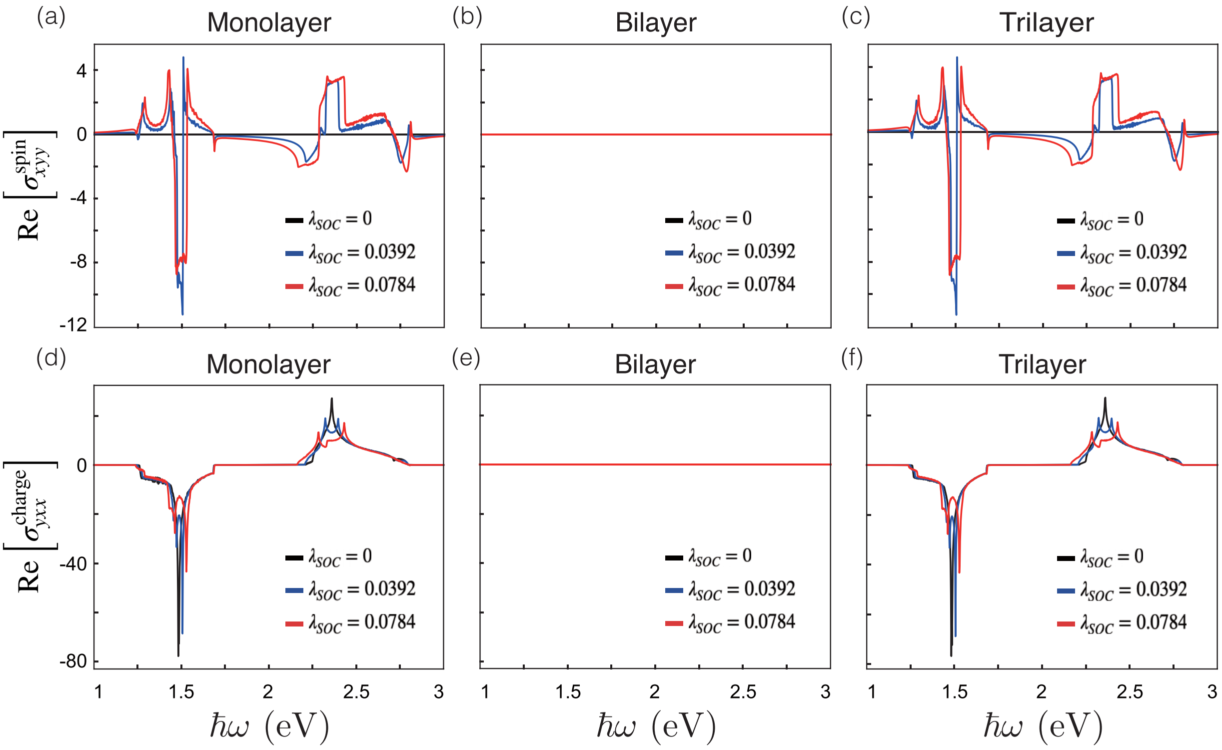

FIG. 2. Real parts of nonlinear optical spin Hall conductivities $\mathrm{Re}[\sigma^{\mathrm{spin}}_{xyy}(\omega,\omega)]$ of (a) monolayer, (b) bilayer, and (c) trilayer $NbSe_2$, respectively. By irradiating y-polarized light, nonlinear optical spin Hall current is generated in odd-number-layered $NbSe_2$. Real parts of nonlinear optical charge Hall conductivities $\mathrm{Re}[\sigma^{\mathrm{charge}}_{yxx}(\omega,\omega)]$ of (d) monolayer, (e) bilayer, and (f) trilayer $NbSe_2$, respectively. Nonlinear optical charge Hall current is generated by x-polarized light irradiation. Red, blue, and black lines indicate several different SOC parameters. The units of nonlinear optical spin and charge Hall conductivities are e^2 and $e^3/\hbar$, respectively.

In addition, a TMDC semiconductor such as MoS_2 has a pronounced peak around 1.75 eV in the nonlinear optical Hall conductivity. The details of nonlinear optical Hall conductivity of monolayer MoS_2 can be found in the Supplemental Material [70]. This transition process corresponds to the SHG process marked with the green arrows in Fig. 5(c) of Appendix A. Thus, SHG can be expected in the doped MoS_2. Similarly, when we consider the case of electron-doped $NbSe_2$ to make the valence bands fully occupied, the system behaves as a semiconductor. In this case, the nonlinear optical conductivity for SHG process has the localized peak around 1.5 eV (not shown). This transition process also corresponds to the SHG process marked with the green arrows in Fig. 5(c) of Appendix A, which is same as the case of MoS_2.

In previous works [54–57] it is reported that the nonlinear charge Hall current in DC limit can be generated even in the absence of magnetic field, by considering monolayer $NbSe_2$ under uniaxial strain or hole-doped semiconductor TMDC. These results can be induced by Berry curvature dipole which provides unconventional behavior, i.e., nonlinear Hall effect, but it is limited to in metallic TMDC. In this work, however, we can show that the nonlinear charge Hall current appears in not only metallic TMDC but also semiconductor TMDC by light irradiation even without SOC and uniaxial strain [see Figs. 2(d) and 2(f)]. Thus, we can generate the nonlinear charge Hall current simply by irradiating light in few-layered $NbSe_2$ without the external perturbations such as magnetic field, strain, and carrier dopings. Figure 3 summarizes the schematics of nonlinear optical Hall currents in few-layered $NbSe_2$ which capture the results of Fig. 2. Figure 3(a) indicates that nonlinear optical spin Hall current is generated in x direction by irradiating y-polarized light in odd-number-layered $NbSe_2$. However, the nonlinear optical charge Hall current is absent. Figure 3(b) shows that the nonlinear optical charge Hall current is generated in y direction by irradiating x-polarized light, but then the spin Hall current is absent. Also, Figs. 3(c) and 3(d) show that because even-number-layered $NbSe_2$ respects inversion symmetry, the nonlinear optical spin and charge Hall currents are identically zero.

IV. ELECTRIC FIELD EFFECT OF NONLINEAR OPTICAL HALL CONDUCTIVITY

Since the application of electric field perpendicular to the plane breaks the crystal inversion symmetry in bilayer $NbSe_2$, the nonlinear optical spin and charge Hall conductivities can be generated even in bilayer $NbSe_2$ with the application of electric field. Figure 4(a) shows the real part of nonlinear optical spin Hall conductivity $\mathrm{Re}[\sigma^{\mathrm{spin}}_{xyy}(\omega,\omega)]$ of bilayer $NbSe_2$ for several different applied electric fields. Here, black, blue, cyan, green, yellow, purple, and red lines indicate the applied electric fields: $F = 0.0$, 0.2, 0.4, 0.6, 0.8, 1.0, and 2.0 eV, respectively. We can see peaks of $\mathrm{Re}[\sigma^{\mathrm{spin}}_{xyy}(\omega,\omega)]$ around 1.5 and 2.5 eV the same as the case of odd-number layer. In addition, there is a pronounced peak which shifts toward higher frequency with the increase of electric field, which is indicated by the dashed square in Fig. 4(a). The peak is originated from the interlayer optical absorption. Since

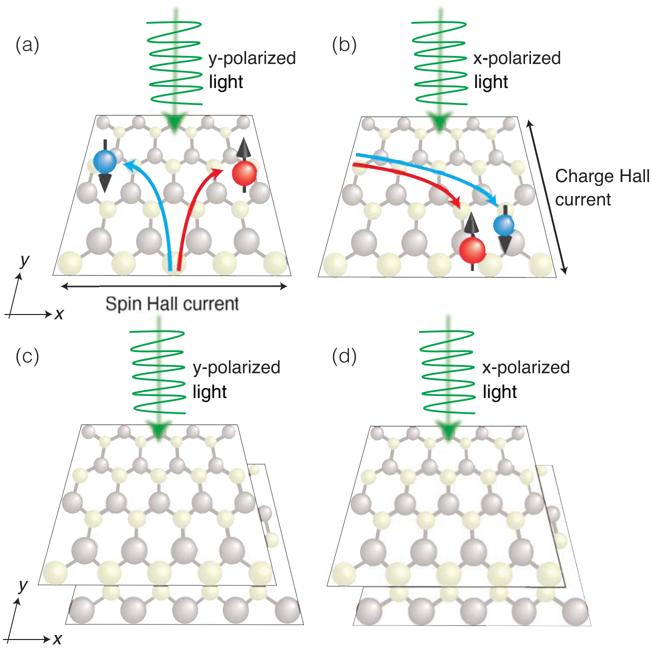

FIG. 3. Schematics of nonlinear optical spin and charge Hall currents in few-layered $NbSe_2$. (a) By y-polarized light irradiation, nonlinear optical spin Hall current is generated in x direction, but nonlinear optical charge Hall current is absent in odd-number-layered $NbSe_2$. (b) By x-polarized light irradiation, nonlinear optical spin Hall current disappears, but nonlinear optical charge Hall current is generated in y direction in odd-number-layered $NbSe_2$. Nonlinear optical (c) spin and (d) charge Hall currents are not generated in even-number-layered $NbSe_2$.

the energy bands of upper (lower) layer shift toward higher (lower) energy, the energy difference between upper and lower layers increases with an increase of electric field, resulting in the shift of interlayer optical absorption peak. The details about energy band structures of bilayer $NbSe_2$ with applied electric fields and its parity between layers are shown in Appendix D.

Figure 4(b) shows the real part of nonlinear optical charge Hall conductivity $\mathrm{Re}[\sigma^{\mathrm{charge}}_{yxx}(\omega,\omega)]$ of bilayer $NbSe_2$ with applied electric fields. Because of the broken crystal inversion symmetry in even-number-layered $NbSe_2$ with applied electric fields, the nonlinear optical charge Hall current can be generated by irradiating x-polarized light. $\mathrm{Re}[\sigma^{\mathrm{charge}}_{yxx}(\omega,\omega)]$ also has peaks around 1.5 and 2.5 eV, which is similar to the case of $\mathrm{Re}[\sigma^{\mathrm{spin}}_{xyy}(\omega,\omega)]$. Similarly, we can observe the frequency shift of interlayer optical absorption peak which is indicated by the dashed squares. Thus, we can indicate that owing to the broken inversion symmetry in even-number-layered $NbSe_2$ with applied electric fields, the nonlinear optical spin and charge Hall currents can be generated by irradiating visible light.

Instead of the application of electric fields to $NbSe_2$, we consider the nonlinear optical spin and charge conductivities of bilayer $NbSe_2$ with each layer having a different Fermi energy, i.e., decoupled bilayer $NbSe_2$. The details of the nonlinear optical spin and charge Hall conductivities of the decoupled bilayer $NbSe_2$ are shown in Appendix E.

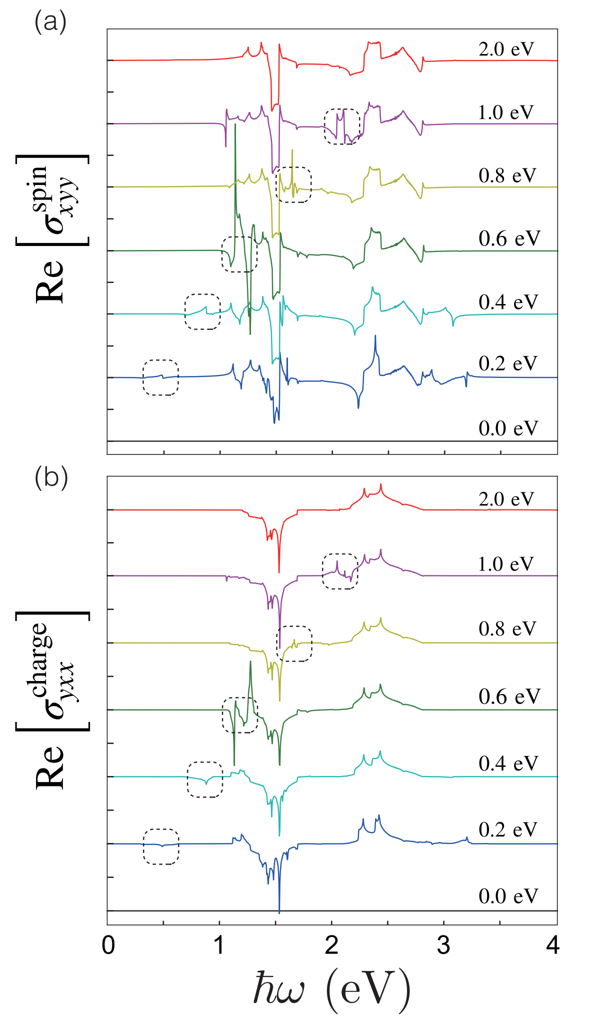

FIG. 4. Nonlinear optical (a) spin and (b) charge Hall conductivities of bilayer $NbSe_2$ for several different applied electric fields. The electric fields are $F = 0.2$ (blue), 0.4 (cyan), 0.6 (green), 0.8 (yellow), 1.0 (purple), and 2.0 eV (red), respectively. (a) By irradiating y-polarized light, the real part of nonlinear optical spin Hall current $\mathrm{Re}[\sigma^{\mathrm{spin}}_{xyy}(\omega,\omega)]$ is generated in bilayer $NbSe_2$ with the application of electric fields. (b) By irradiating x-polarized light, the real part of nonlinear optical charge Hall current $\mathrm{Re}[\sigma^{\mathrm{charge}}_{yxx}(\omega,\omega)]$ is generated in bilayer $NbSe_2$. The units of nonlinear optical spin and charge Hall conductivities are e^2 and $e^3/\hbar$, respectively.

V. CONCLUSION

In conclusion, we have theoretically proposed that nonlinear optical spin and charge Hall currents based on the SHG process can be enhanced by irradiating visible light. Also, we have shown that the Hall currents strongly depend on layer numbers, crystal symmetry of $NbSe_2$, and polarization of incident light, i.e., nonlinear optical selection rule of spin and charge Hall currents in few-layered $NbSe_2$. In previous works, it is known that the nonlinear Hall effect is induced in metallic and doped semiconductor TMDCs by uniaxial strain, which depends on the Berry curvature dipole in the first BZ. In our work we can find nonlinear Hall effect by light irradiation in $NbSe_2$ and MoS_2 with hole doping, even in the absence of strain. In the Supplemental Material [70], it is also shown that the nonlinear optical spin and charge Hall conductivities can occur in MoS_2 without doping. Thus, in general, it is expected that the nonlinear optical Hall effect can occur in TMDC materials.

In addition, we have found that the nonlinear optical spin and charge Hall currents of few-layered $NbSe_2$ based on the effective TBM are robust to temperature and are expected to be observed even at room temperature (see the Supplemental Material [70]).

In this paper we have found that the oscillating spin and charge Hall current could be induced by the SHG. Though the static charge and spin accumulation does not occur, the polarized spin current can be extracted if we attach the half-metal materials to the edge of the sample as a spin filter.

Thus, few-layered $NbSe_2$ can be used for the source of induced nonlinear optical spin Hall current by SHG. Our results can serve to design opt-spintronics devices on the basis of 2D materials.

ACKNOWLEDGMENTS

This work was supported by JSPS KAKENHI (No. JP21H01019 and No. JP18H01154) and JST CREST (No. JPMJCR19T1).

APPENDIX A: MATRIX ELEMENTS OF FEW-LAYERED $NbSe_2$

We employ a multiorbitals TBM which includes d_{z^2}, $d_{x^2-y^2}$, and d_{xy} orbitals of Nb atom to describe the electronic states of $NbSe_2$. The eigenvalue equation for TBM is $\hat{H}(\boldsymbol{k})|u_{n\boldsymbol{k}}\rangle = E_{n\boldsymbol{k}}|u_{n\boldsymbol{k}}\rangle$, where $\boldsymbol{k} = (k_x, k_y)$ is the wave-number vector, $E_{n\boldsymbol{k}}$ is the eigenvalue, and $n = 1, 2, \dots, 6N$ (N is the number of layers) is the band index. The eigenvector is defined as $|u_{n\boldsymbol{k}}\rangle = (c_{n\boldsymbol{k},d_{z^2},\uparrow}, c_{n\boldsymbol{k},d_{xy},\uparrow}, c_{n\boldsymbol{k},d_{x^2-y^2},\uparrow}, c_{n\boldsymbol{k},d_{z^2},\downarrow}, c_{n\boldsymbol{k},d_{xy},\downarrow}, c_{n\boldsymbol{k},d_{x^2-y^2},\downarrow})^T$, where $(\cdots)^T$ indicates the transpose of vector and $c_{n\boldsymbol{k}\tau s}$ means the amplitude at atomic orbital τ with spin s for the nth energy band at $\boldsymbol{k}$. The Hamiltonian of monolayer $NbSe_2$ with Ising-type SOC can be written as

$$\hat{H}_{\rm mono}(\boldsymbol{k}) = \hat{\sigma}_0 \otimes \hat{H}_{\rm TNN}(\boldsymbol{k}) + \hat{\sigma}_z \otimes \tfrac{1}{2}\lambda_{\rm SOC}\hat{L}_z, \tag{A1}$$

with

$$\hat{H}_{\rm TNN}(\boldsymbol{k}) = \begin{pmatrix} V_0 & V_1 & V_2 \\ V_1^* & V_{11} & V_{12} \\ V_2^* & V_{12}^* & V_{22} \end{pmatrix} \tag{A2}$$

and

$$\hat{L}_z = \begin{pmatrix} 0 & 0 & 0 \\ 0 & 0 & -2i \\ 0 & 2i & 0 \end{pmatrix}. \tag{A3}$$

Here $\hat{\sigma}_0$ and $\hat{\sigma}_z$ are Pauli matrices and $\lambda_{\rm SOC}$ is the Ising-type SOC parameter. In monolayer $NbSe_2$, $\lambda_{\rm SOC} = 0.0784$ eV. $\hat{H}_{\rm TNN}(\boldsymbol{k})$ includes the electron hoppings only among three d orbitals of Nb atoms, which are assumed up to third-nearest neighbor sites as shown in Fig. 5(a). Here, green, red, and blue arrows indicate hopping vectors $\boldsymbol{R_i}$ ($i = 1, 2, \dots, 6$) pointing to nearest-neighbor (nn) sites, the vectors $\tilde{\boldsymbol{R}}_{\boldsymbol{j}}$ ($j = 1, 2, \dots, 6$) pointing to next nn sites, and the vectors $2\boldsymbol{R_i}$ pointing to third nn sites, respectively. We can find the matrix elements in the effective TBM Hamiltonian of monolayer $NbSe_2$ [71,82]: V_0, V_1, V_2, V_{11}, V_{12}, and V_{22} as

$$\begin{aligned} V_0 = {} & \varepsilon_1 + 2t_0(2\cos\alpha\cos\beta + \cos 2\alpha) \\ & + 2r_0(2\cos 3\alpha\cos\beta + \cos 2\beta) \\ & + 2u_0(2\cos 2\alpha\cos 2\beta + \cos 4\alpha), \end{aligned} \tag{A4}$$

$$\begin{aligned} {\rm Re}[V_1] = {} & -2\sqrt{3}t_2\sin\alpha\sin\beta + 2(r_1 + r_2)\sin 3\alpha\sin\beta \\ & - 2\sqrt{3}u_2\sin 2\alpha\sin 2\beta, \end{aligned} \tag{A5}$$

$$\begin{aligned} {\rm Im}[V_1] = {} & 2t_1\sin\alpha(2\cos\alpha + \cos\beta) + 2(r_1 - r_2)\sin 3\alpha\cos\beta \\ & + 2u_1\sin 2\alpha(2\cos 2\alpha + \cos 2\beta), \end{aligned} \tag{A6}$$

$$\begin{aligned} {\rm Re}[V_2] = {} & 2t_2(\cos 2\alpha - \cos\alpha\cos\beta) \\ & - \frac{2}{\sqrt{3}}(r_1 + r_2)(\cos 3\alpha\cos\beta - \cos 2\beta) \\ & + 2u_2(\cos 4\alpha - \cos 2\alpha\cos 2\beta), \end{aligned} \tag{A7}$$

$$\begin{aligned} {\rm Im}[V_2] = {} & 2\sqrt{3}t_1\cos\alpha\sin\beta \\ & + \frac{2}{\sqrt{3}}(r_1 - r_2)\sin\beta(\cos 3\alpha + 2\cos\beta) \\ & + 2\sqrt{3}u_1\cos 2\alpha\sin 2\beta, \end{aligned} \tag{A8}$$

$$\begin{aligned} V_{11} = {} & \varepsilon_2 + (t_{11} + 3t_{22})\cos\alpha\cos\beta + 2t_{11}\cos 2\alpha \\ & + 4r_{11}\cos 3\alpha\cos\beta + 2(r_{11} + \sqrt{3}r_{12})\cos 2\beta \\ & + (u_{11} + 3u_{22})\cos 2\alpha\cos 2\beta + 2u_{11}\cos 4\alpha, \end{aligned} \tag{A9}$$

$$\begin{aligned} {\rm Re}[V_{12}] = {} & \sqrt{3}(t_{22} - t_{11})\sin\alpha\sin\beta + 4r_{12}\sin 3\alpha\sin\beta \\ & + \sqrt{3}(u_{22} - u_{11})\sin 2\alpha\sin 2\beta, \end{aligned} \tag{A10}$$

$$\begin{aligned} {\rm Im}[V_{12}] = {} & 4t_{12}\sin\alpha(\cos\alpha - \cos\beta) \\ & + 4u_{12}\sin 2\alpha(\cos 2\alpha - \cos 2\beta), \end{aligned} \tag{A11}$$

and

$$\begin{aligned} V_{22} = {} & \varepsilon_2 + (3t_{11} + t_{22})\cos\alpha\cos\beta + 2t_{22}\cos 2\alpha \\ & + 2r_{11}(2\cos 3\alpha\cos\beta + \cos 2\beta) \\ & + \frac{2}{\sqrt{3}}r_{12}(4\cos 3\alpha\cos\beta - \cos 2\beta) \\ & + (3u_{11} + u_{22})\cos 2\alpha\cos 2\beta + 2u_{22}\cos 4\alpha. \end{aligned} \tag{A12}$$

Here $(\alpha, \beta) = (\frac{1}{2}k_x a, \frac{\sqrt{3}}{2}k_y a)$ and the lattice constant a is 3.45 Å. The specific hopping parameters in this TBM can be given as

$$E^{jj'}_{\mu\mu'}(\boldsymbol{R}) = \langle\psi^j_\mu(\boldsymbol{r})|\hat{H}(\boldsymbol{k})|\phi^{j'}_{\mu'}(\boldsymbol{r} - \boldsymbol{R})\rangle\,, \tag{A13}$$

where $|u_{n\boldsymbol{k}}\rangle \to |\phi^j_\mu\rangle$ indicates an atomic orbital of Nb atom and in this paper we consider $|\phi^1_1\rangle = d_{z^2}$, $|\phi^2_1\rangle = d_{xy}$, and $|\phi^2_2\rangle = d_{x^2-y^2}$. For example, we can express $t_0 = E^{11}_{11}(\boldsymbol{R_1})$, $t_1 = E^{12}_{11}(\boldsymbol{R_1})$, $r_0 = E^{11}_{11}(\tilde{\boldsymbol{R}}_{\boldsymbol{1}})$, $r_1 = E^{12}_{11}(\tilde{\boldsymbol{R}}_{\boldsymbol{1}})$, $u_0 = E^{11}_{11}(2\boldsymbol{R_1})$, and $u_1 = E^{12}_{11}(2\boldsymbol{R_1})$.

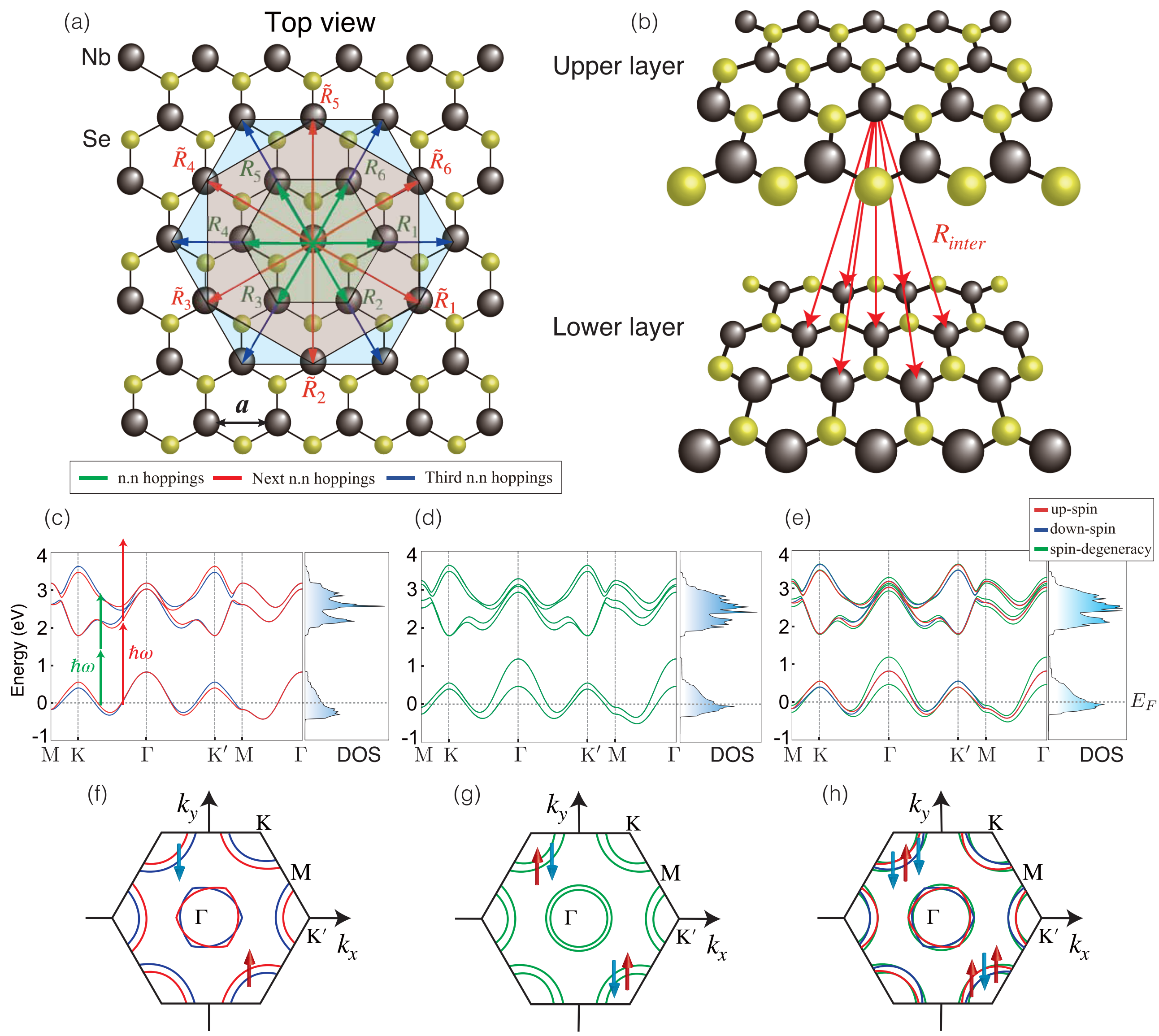

FIG. 5. (a) Top view of crystal structure of monolayer $NbSe_2$ which consists of Nb (black) and Se (yellow) atoms. Green, red, and blue arrows indicate hopping vectors $\boldsymbol{R}_i$ ($i = 1, 2, \ldots, 6$) pointing to nn sites, the vectors $\tilde{\boldsymbol{R}}_j$ ($j = 1, 2, \ldots, 6$) pointing to next nn sites and the vectors $2\boldsymbol{R}_i$ pointing to third nn sites, respectively. a is the lattice constant. (b) Side view of crystal structure of bilayer $NbSe_2$. Interlayer hopping vector $\boldsymbol{R}_{\text{inter}}$ points from the d orbital of the upper layer to nn sites of the lower layer. Energy band structures and DOS of (c) monolayer, (d) bilayer, and (e) trilayer $NbSe_2$ with SOC parameter $\lambda_{\text{SOC}} = 0.0784\,\text{eV}$, respectively. Fermi level is set to zero. The arrows in (c) include the two SHG processes: (i) interband transition by two-photon absorption (green arrows) and (ii) interband transition even by one-photon absorption (red arrows). Fermi surface of (f) monolayer, (g) bilayer, and (h) trilayer $NbSe_2$, where red, blue, and green lines indicate for up-spin, down-spin, and spin-degenerated states, respectively.

Similarly, Hamiltonians of (AB-stacked) bilayer and (ABA-stacked) trilayer $NbSe_2$ can be obtained as

$$\hat{H}_{\text{bi}}(\boldsymbol{k}) = \begin{pmatrix} \hat{H}_{\text{mono}}(-\boldsymbol{k}) & \hat{H}_{\text{int}}(\boldsymbol{k}) \\ \hat{H}^{\dagger}_{\text{int}}(\boldsymbol{k}) & \hat{H}_{\text{mono}}(\boldsymbol{k}) \end{pmatrix} \tag{A14}$$

and

$$\hat{H}_{\text{tri}}(\boldsymbol{k}) = \begin{pmatrix} \hat{H}_{\text{mono}}(\boldsymbol{k}) & \hat{H}_{\text{int}}(\boldsymbol{k}) & 0 \\ \hat{H}^{\dagger}_{\text{int}}(\boldsymbol{k}) & \hat{H}_{\text{mono}}(-\boldsymbol{k}) & \hat{H}_{\text{int}}(\boldsymbol{k}) \\ 0 & \hat{H}^{\dagger}_{\text{int}}(\boldsymbol{k}) & \hat{H}_{\text{mono}}(\boldsymbol{k}) \end{pmatrix}, \tag{A15}$$

respectively. In Fig. 5(b), interlayer hopping vector $\boldsymbol{R}_{\text{inter}}$ points the d orbital of the upper layer to nn sites of the lower layer and the interlayer coupling Hamiltonian $\hat{H}_{\text{int}}(\boldsymbol{k})$ is considered as

$$\hat{H}_{\text{int}}(\boldsymbol{k}) = \begin{pmatrix} T_{01} & 0 & 0 \\ 0 & T_{02} & 0 \\ 0 & 0 & T_{02} \end{pmatrix}, \tag{A16}$$

where T_{01} and T_{02} are fitted by using hopping parameters t_{01} and t_{02}:

$$T_{01} = 3t_{01} + 2t_{01}(2\cos\alpha\cos\beta + \cos 2\alpha), \tag{A17}$$

$$T_{02} = t_{02}, \tag{A18}$$

TABLE II. Fitting parameters for the effective TBM Hamiltonian of few-layered $NbSe_2$. The energy parameters ϵ_1 to λ_{SOC} are in units of eV.

ϵ_1	ϵ_2	t_0	t_1	t_2	t_{11}	t_{12}	t_{22}	r_0	r_1	r_2
r_{11}	r_{12}	u_0	u_1	u_2	u_{11}	u_{12}	u_{22}	t_{01}	t_{02}	λ_{SOC}
1.4466	1.8496	−0.2308	0.3116	0.3459	0.2795	0.2787	−0.0539	0.0037	−0.0997	0.0385
0.0320	0.0986	0.1233	−0.0381	0.0535	0.0601	−0.0179	−0.0425	−0.0179	−0.0702	0.0784

respectively. The details about fitted parameters for this TBM are summarized in Table II [60].

The energy band structures and DOS are shown in Figs. 5(c)–5(e). Here, red, blue, and green lines indicate spin-up, spin-down, and spin-degenerated states, respectively. The energy band structure of monolayer $NbSe_2$ is qualitatively similar to heavily hole-doped monolayer MoS_2. Unlike monolayer MoS_2 which shows semiconducting behavior, monolayer $NbSe_2$ is metallic, but with a large energy band gap between the partially filled valence bands and empty conduction bands. Also, the Ising-type SOC provides opposite spin splitting at the valence band edges in K and K' points, and time-reversal symmetry protection. In particular, the SOC makes the spin splitting about 157 meV at the K point. Figure 5(d) shows that the spin splitting is absent in the energy band structure of bilayer $NbSe_2$, but larger band splitting appears at the valence band in Γ point because of the spacial inversion symmetry. Figure 5(e) shows that trilayer $NbSe_2$ has spin splitting bands owing to the broken crystal inversion symmetry the same as the case of monolayer. In general, the energy band structures of $NbSe_2$ have spin degeneracy along the Γ-M line, which can be confirmed by looking at Fermi surface structure. Also, this is because the Hamiltonians for up- and down-spin states have the following properties: $\hat{H}^{\uparrow}_{\rm mono}(\boldsymbol{k}) = (\hat{H}^{\downarrow}_{\rm mono}(\boldsymbol{k}))^{\dagger}$, $\hat{H}^{\uparrow}_{\rm bi}(\boldsymbol{k}) = (\hat{H}^{\downarrow}_{\rm bi}(\boldsymbol{k}))^{\dagger}$, and $\hat{H}^{\uparrow}_{\rm tri}(\boldsymbol{k}) = (\hat{H}^{\downarrow}_{\rm tri}(\boldsymbol{k}))^{\dagger}$, respectively. Since we have interest in the SHG, we discuss the nonlinear optical conductivity for SHG process ($\omega_1 = \omega_2 = \omega$). Figure 5(c) includes the two SHG processes: (i) interband transition by two-photon absorption (green arrows) and (ii) interband transition even by one-photon absorption (red arrows).

Figure 5(f) shows Fermi surface of monolayer $NbSe_2$. The surface has Fermi pockets centered at Γ, K, and K' points, which show the spin splitting. Also, because of the opposite spin splitting around K and K' points, the energy band structure of monolayer $NbSe_2$ is anisotropic with respect to Γ point. Figure 5(g) indicates the Fermi surface of bilayer $NbSe_2$. Unlike the case of monolayer, the surface has spin-degenerated Fermi pockets owing to the crystal inversion symmetry. Figure 5(h) shows Fermi surface of trilayer $NbSe_2$, which has spin-splitting Fermi surface. This Fermi surface can be understood by overlaying the spin-splitting Fermi surface of monolayer $NbSe_2$ on the spin-degenerated Fermi surface of bilayer $NbSe_2$. We can mention that the spin dependence of the Fermi surface behaves differently for even- and odd-number-layered $NbSe_2$.

APPENDIX B: BERRY CURVATURE DIPOLE IN NONLINEAR OPTICAL CONDUCTIVITY

We numerically calculate nonlinear optical spin and charge Hall conductivities of SHG process for few-layered $NbSe_2$ based on an effective TBM. In general, the second order nonlinear optical conductivity σ_{ijk} can be given as

$$\sigma_{ijk}(\omega_1,\omega_2) = -\frac{\hbar^2 e^2}{S}\sum_{\boldsymbol{k}}\sum_{nml}\frac{1}{E_{ml}E_{ln}(E_{mn}-\hbar\omega_1-\hbar\omega_2-i\eta)}\left[\frac{\langle u_{n\boldsymbol{k}}|\hat{v}_j|u_{l\boldsymbol{k}}\rangle\langle u_{l\boldsymbol{k}}|\hat{v}_k|u_{m\boldsymbol{k}}\rangle\langle u_{m\boldsymbol{k}}|\hat{j}_i|u_{n\boldsymbol{k}}\rangle f_{ml}}{E_{ml}-\hbar\omega_2-i\eta} - \frac{\langle u_{n\boldsymbol{k}}|\hat{v}_k|u_{l\boldsymbol{k}}\rangle\langle u_{l\boldsymbol{k}}|\hat{v}_j|u_{m\boldsymbol{k}}\rangle\langle u_{m\boldsymbol{k}}|\hat{j}_i|u_{n\boldsymbol{k}}\rangle f_{ln}}{E_{ln}-\hbar\omega_2-i\eta}\right], \tag{B1}$$

where $i(j,k)$ indicates the direction x or y. In particular, the case where ijk is xyy and yxx is called as Hall conductivity. Also, $n(m,l)$ is the band index including spin degree of freedom, $|u_{n\boldsymbol{k}}\rangle$ is the eigenfunction with the eigenenergy $E_{n\boldsymbol{k}}$, and $f(E_{n\boldsymbol{k}})$ is the Fermi-Dirac distribution function. $E_{ml} \equiv E_m - E_l$, $f_{ml} \equiv f(E_{m\boldsymbol{k}}) - f(E_{l\boldsymbol{k}})$, η is infinitesimally small real number, and S is the area of system. $\hat{j}_i$ can be defined for spin and charge current operators, which can be written as $\hat{j}_i^{\rm spin} = \frac{1}{2}\{\frac{\hbar}{2}\hat{\sigma}_z\otimes\hat{I}_N, \hat{v}_i\}$ and $\hat{j}_i^{\rm charge} = \frac{1}{2}\{-e\hat{\sigma}_0\otimes\hat{I}_N, \hat{v}_i\}$, respectively. Here $\hat{I}_N$ is the $N\times N$ identity matrix and $N = 3, 6, 9$ is used for monolayer, bilayer, and trilayer $NbSe_2$, respectively. Moreover, $\hat{v}_i = \frac{1}{\hbar}\frac{\partial\hat{H}}{\partial i}$ is the group velocity operator. We add the superscript "spin" for the nonlinear optical spin conductivity $\sigma_{ijk}^{\rm spin}(\omega,\omega)$ in order to distinguish its conductivity from the nonlinear optical charge conductivity $\sigma_{ijk}^{\rm charge}(\omega,\omega)$. In the case of $\omega_1 = \omega_2 = \omega$, the process is called SHG. In addition, in the case of $\omega_1 + \omega_2 = \omega_3$, the process is called SFG.

The second order nonlinear optical conductivity expressed by Eq. (B1) can be separated into two interband processes using the following identity:

$$\frac{1}{(\hbar\omega_1+\hbar\omega_2+i\eta)(\hbar\omega_{mn}-\hbar\omega_1-\hbar\omega_2-i\eta)} = \frac{1}{(\hbar\omega_1+\hbar\omega_2+i\eta)\hbar\omega_{mn}} + \frac{1}{\hbar\omega_{mn}(\hbar\omega_{mn}-\hbar\omega_1-\hbar\omega_2-i\eta)}, \tag{B2}$$

where the first term leads to (i) optical transition between two bands $\sigma_{ijk}^{(2)}$ and the second term corresponds to (ii) optical transition involving three bands $\sigma_{ijk}^{(3)}$ [76,80]. Namely, σ_{ijk} can be decomposed into

$$\sigma_{ijk}(\omega_1, \omega_2) = \sigma_{ijk}^{(2)}(\omega_1, \omega_2) + \sigma_{ijk}^{(3)}(\omega_1, \omega_2). \tag{B3}$$

In particular, $\sigma_{ijk}^{(2)}$ can be given as

$$\sigma_{ijk}^{(2)}(\omega_1, \omega_2) = \frac{\hbar^2 e^2}{S}\sum_{\boldsymbol{k}}\sum_{nml}\frac{1}{E_{ml}E_{ln}E_{mn}}\left[\frac{\langle u_{n\boldsymbol{k}}|\hat{v}_j|u_{l\boldsymbol{k}}\rangle\,\langle u_{l\boldsymbol{k}}|\hat{v}_k|u_{m\boldsymbol{k}}\rangle\,\langle u_{m\boldsymbol{k}}|\hat{j}_i|u_{n\boldsymbol{k}}\rangle\, f_{ml}}{E_{ml}-\hbar\omega_2-i\eta} - \frac{\langle u_{n\boldsymbol{k}}|\hat{v}_k|u_{l\boldsymbol{k}}\rangle\,\langle u_{l\boldsymbol{k}}|\hat{v}_j|u_{m\boldsymbol{k}}\rangle\,\langle u_{m\boldsymbol{k}}|\hat{j}_i|u_{n\boldsymbol{k}}\rangle\, f_{ln}}{E_{ln}-\hbar\omega_2-i\eta}\right]. \tag{B4}$$

Moreover, we can express $\sigma_{ijk}^{(2)}$ simply as interband transition between valence band n and conduction band m using the following relations:

$$\hbar^2\sum_{l}\left(\frac{\langle u_{n\boldsymbol{k}}|\hat{v}_k|u_{l\boldsymbol{k}}\rangle\,\langle u_{l\boldsymbol{k}}|\hat{v}_j|u_{m\boldsymbol{k}}\rangle}{E_{ln}E_{ml}} - \frac{\langle u_{n\boldsymbol{k}}|\hat{v}_j|u_{l\boldsymbol{k}}\rangle\,\langle u_{l\boldsymbol{k}}|\hat{v}_k|u_{m\boldsymbol{k}}\rangle}{E_{ln}E_{ml}}\right) = \left(\frac{\langle u_{n\boldsymbol{k}}|\hat{v}_j|u_{m\boldsymbol{k}}\rangle}{\omega_{nm}}\right)_{;k^k} - \left(\frac{\langle u_{n\boldsymbol{k}}|\hat{v}_k|u_{m\boldsymbol{k}}\rangle}{\omega_{nm}}\right)_{;k^j}, \tag{B5}$$

where

$$\begin{aligned}\left(\frac{\langle u_{n\boldsymbol{k}}|\hat{v}_\alpha|u_{m\boldsymbol{k}}\rangle}{\omega_{nm}}\right)_{;k^\beta} &= \frac{\langle u_{n\boldsymbol{k}}|\hat{v}_\beta|u_{m\boldsymbol{k}}\rangle\,\langle u_{m\boldsymbol{k}}|\hat{\Delta}_\alpha|u_{n\boldsymbol{k}}\rangle + \langle u_{n\boldsymbol{k}}|\hat{v}_\alpha|u_{m\boldsymbol{k}}\rangle\,\langle u_{m\boldsymbol{k}}|\hat{\Delta}_\beta|u_{n\boldsymbol{k}}\rangle}{i\omega_{nm}^2}\\ &\quad + \frac{i\hbar}{\omega_{nm}}\sum_l\left(\frac{\langle u_{n\boldsymbol{k}}|\hat{v}_\beta|u_{l\boldsymbol{k}}\rangle\,\langle u_{l\boldsymbol{k}}|\hat{v}_\alpha|u_{m\boldsymbol{k}}\rangle}{E_{ln}} - \frac{\langle u_{n\boldsymbol{k}}|\hat{v}_\alpha|u_{l\boldsymbol{k}}\rangle\,\langle u_{l\boldsymbol{k}}|\hat{v}_\beta|u_{m\boldsymbol{k}}\rangle}{E_{ml}}\right).\end{aligned} \tag{B6}$$

Here $\langle u_{m\boldsymbol{k}}|\hat{\Delta}_j|u_{n\boldsymbol{k}}\rangle \equiv \langle u_{m\boldsymbol{k}}|\hat{v}_j|u_{m\boldsymbol{k}}\rangle - \langle u_{n\boldsymbol{k}}|\hat{v}_j|u_{n\boldsymbol{k}}\rangle$ and $\alpha(\beta)$ is the direction x or y. In other words, $\sigma_{ijk}^{(2)}$ can be rewritten as

$$\begin{aligned}\sigma_{ijk}^{(2)}(\omega_1, \omega_2) &= -\frac{ie^2}{S}\frac{1}{\hbar\omega_1+\hbar\omega_2+i\eta}\sum_{\boldsymbol{k}}\sum_{n} i\hbar^2\sum_{m\neq n}\frac{\langle u_{n\boldsymbol{k}}|\hat{v}_j|u_{m\boldsymbol{k}}\rangle\,\langle u_{m\boldsymbol{k}}|\hat{v}_k|u_{n\boldsymbol{k}}\rangle}{(E_{m\boldsymbol{k}}-E_{n\boldsymbol{k}})^2}\,\langle u_{n\boldsymbol{k}}|\hat{j}_i|u_{n\boldsymbol{k}}\rangle\,\frac{f_{mn}}{E_{mn}-\hbar\omega_2-i\eta}\\ &= -\frac{ie^2}{S}\frac{1}{\hbar\omega_1+\hbar\omega_2+i\eta}\sum_{\boldsymbol{k}}\sum_{n}\Omega_n(\boldsymbol{k})\,\langle u_{n\boldsymbol{k}}|\hat{j}_i|u_{n\boldsymbol{k}}\rangle\,\frac{f_{mn}}{E_{mn}-\hbar\omega_2-i\eta},\end{aligned} \tag{B7}$$

where $\Omega_n(\boldsymbol{k})$ is the Berry curvature, i.e.,

$$\Omega_n(\boldsymbol{k}) = i\hbar^2\sum_{m\neq n}\frac{\langle u_{n\boldsymbol{k}}|\hat{v}_j|u_{m\boldsymbol{k}}\rangle\,\langle u_{m\boldsymbol{k}}|\hat{v}_k|u_{n\boldsymbol{k}}\rangle}{(E_{m\boldsymbol{k}}-E_{n\boldsymbol{k}})^2}. \tag{B8}$$

When we consider the interband transition between two bands around the Fermi surface, $\hbar\omega_2$ in Eq. (B7) is infinitesimally zero, i.e.,

$$\begin{aligned}\sigma_{ijk}^{(2)}(\omega_1, \omega_2\to 0) &= -\frac{ie^2}{S}\frac{1}{\hbar\omega_1+i\eta}\sum_{\boldsymbol{k}}\sum_{n}\Omega_n(\boldsymbol{k})\,\langle u_{n\boldsymbol{k}}|\hat{j}_i|u_{n\boldsymbol{k}}\rangle\,\frac{f_{mn}}{E_{mn}}\\ &= -\frac{ie^2}{S}\frac{1}{\hbar\omega_1+i\eta}\sum_{\boldsymbol{k}}\sum_{n}\Omega_n(\boldsymbol{k})\,\langle u_{n\boldsymbol{k}}|\hat{j}_i|u_{n\boldsymbol{k}}\rangle\,\frac{\partial f_{n\boldsymbol{k}}}{\partial E_{n\boldsymbol{k}}}\\ &= -\frac{ie^2}{S}\frac{1}{\hbar\omega_1+i\eta}D_i,\end{aligned} \tag{B9}$$

where D_i is the Berry curvature dipole [81] and we have used an approximation to Fermi-Dirac distribution

$$f_{mn} = f_{m\boldsymbol{k}} - f_{n\boldsymbol{k}} \approx \frac{\partial f_{n\boldsymbol{k}}}{\partial E_{n\boldsymbol{k}}}(E_{m\boldsymbol{k}}-E_{n\boldsymbol{k}}). \tag{B10}$$

It should be noted that $\sigma_{ijk}^{(2)}$ includes $\Omega_n(\boldsymbol{k})$, velocity and energy derivative of the Fermi-Dirac distribution function. Also, $\sigma_{ijk}^{(3)}$ can be given as

$$\begin{aligned}\sigma_{ijk}^{(3)}(\omega_1, \omega_2) = \frac{\hbar^2 e^2}{S}\sum_{\boldsymbol{k}}\sum_{nml}\frac{\hbar\omega_1+\hbar\omega_2+i\eta}{E_{ml}E_{ln}E_{mn}(E_{mn}-\hbar\omega_1-\hbar\omega_2-i\eta)}&\left[\frac{\langle u_{n\boldsymbol{k}}|\hat{v}_j|u_{l\boldsymbol{k}}\rangle\,\langle u_{l\boldsymbol{k}}|\hat{v}_k|u_{m\boldsymbol{k}}\rangle\,\langle u_{m\boldsymbol{k}}|\hat{j}_i|u_{n\boldsymbol{k}}\rangle\, f_{ml}}{E_{ml}-\hbar\omega_2-i\eta}\right.\\ &\left.-\frac{\langle u_{n\boldsymbol{k}}|\hat{v}_k|u_{l\boldsymbol{k}}\rangle\,\langle u_{l\boldsymbol{k}}|\hat{v}_j|u_{m\boldsymbol{k}}\rangle\,\langle u_{m\boldsymbol{k}}|\hat{j}_i|u_{n\boldsymbol{k}}\rangle\, f_{ln}}{E_{ln}-\hbar\omega_2-i\eta}\right],\end{aligned} \tag{B11}$$

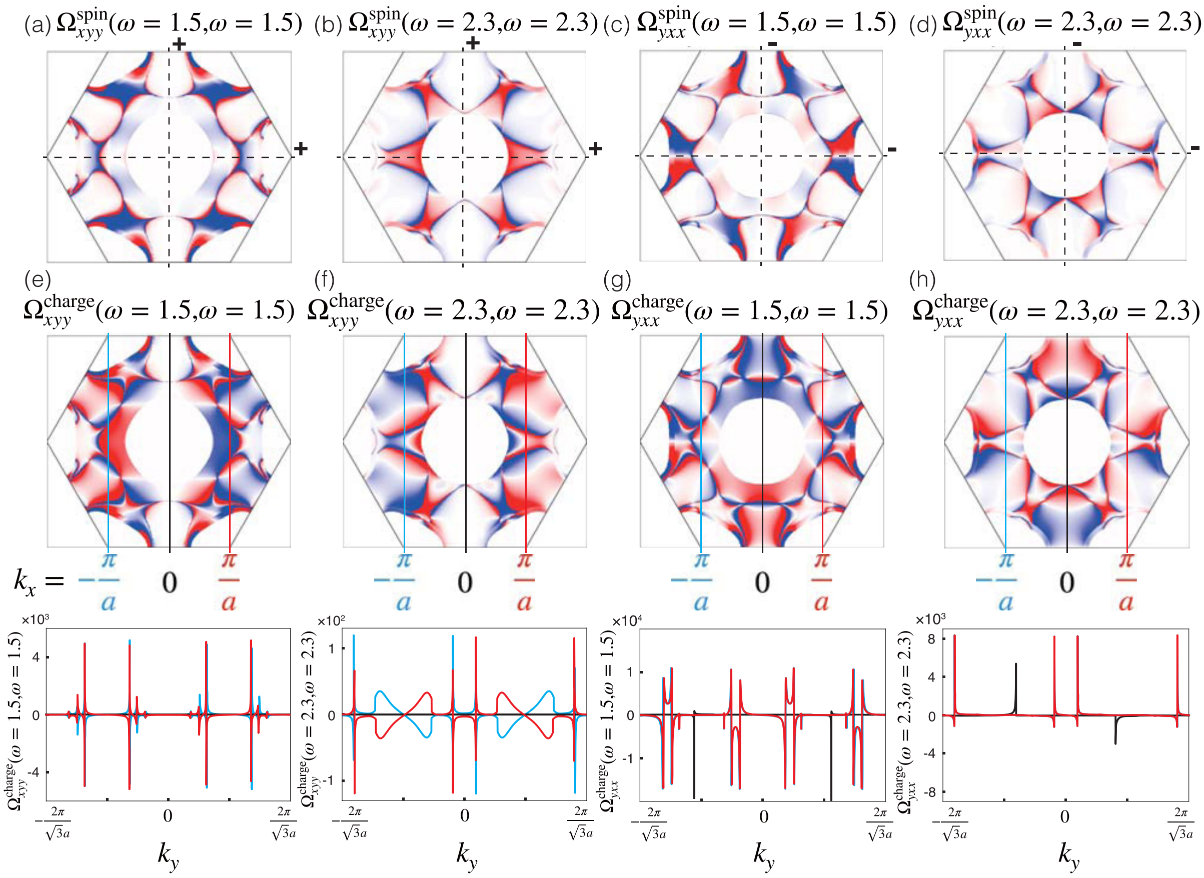

FIG. 6. Contour plots of integrands for nonlinear optical spin Hall conductivities of monolayer $NbSe_2$ in the first BZ: (a) $\Omega^{spin}_{xyy}(\omega = 1.5, \omega = 1.5)$, (b) $\Omega^{spin}_{xyy}(\omega = 2.3, \omega = 2.3)$, (c) $\Omega^{spin}_{yxx}(\omega = 1.5, \omega = 1.5)$, and (d) $\Omega^{spin}_{yxx}(\omega = 2.3, \omega = 2.3)$. Same plots of integrands for nonlinear optical charge Hall conductivities of monolayer $NbSe_2$: (e) $\Omega^{charge}_{xyy}(\omega = 1.5, \omega = 1.5)$, (f) $\Omega^{charge}_{xyy}(\omega = 2.3, \omega = 2.3)$, (g) $\Omega^{charge}_{yxx}(\omega = 1.5, \omega = 1.5)$, and (h) $\Omega^{charge}_{yxx}(\omega = 2.3, \omega = 2.3)$.

where $\sigma^{(3)}_{ijk}$ includes three bands, i.e., a valence band n, an intermediate band l, and a conduction band m.

APPENDIX C: INTEGRANDS OF NONLINEAR OPTICAL SPIN AND CHARGE HALL CONDUCTIVITIES

We calculate integrands of nonlinear optical spin Hall conductivities $\Omega^{spin}_{xyy}(\omega, \omega, \boldsymbol{k})$ and $\Omega^{spin}_{yxx}(\omega, \omega, \boldsymbol{k})$ of few-layered $NbSe_2$. According to Fig. 2, the nonlinear optical spin Hall conductivity of even-number-layered $NbSe_2$ is absent owing to Neumann's principle, but that of odd-number-layered $NbSe_2$ has finite values. Here we especially discuss the case of monolayer. Figures 6(a) and 6(b) show the contour plots of $\Omega^{spin}_{xyy}(\omega, \omega, \boldsymbol{k})$ at $\hbar\omega = 1.5$ and 2.3 eV, respectively. Under light irradiation, $\Omega^{spin}_{xyy}(\omega, \omega, \boldsymbol{k})$ has even parity with respect to k_x and k_y axes. Thus, the k integration of $\Omega^{spin}_{xyy}(\omega, \omega, \boldsymbol{k})$ over the first BZ becomes nonvanishing and reproduces the result of Fig. 2(a). On the other hand, Figs. 6(c) and 6(d) show $\Omega^{spin}_{yxx}(\omega, \omega, \boldsymbol{k})$ under light irradiation of $\hbar\omega = 1.5$ and 2.3 eV, which has odd parity for k_x and k_y axes. Owing to the antisymmetric properties of $\Omega^{spin}_{yxx}(\omega, \omega, \boldsymbol{k})$ for monolayer $NbSe_2$, their k integration over the first BZ has finite value and is consistent with the result of Sec. III. Thus, the nonlinear optical spin Hall current can be generated in x direction for monolayer $NbSe_2$ by irradiating y-polarized light.

Next we discuss $\Omega^{charge}_{xyy}(\omega, \omega, \boldsymbol{k})$ and $\Omega^{charge}_{yxx}(\omega, \omega, \boldsymbol{k})$ of odd-number-layered $NbSe_2$. Owing to the crystal symmetry, Neumann's principle illustrates that the nonlinear optical charge Hall current is absent (generated) in even (odd)-number-layered $NbSe_2$. Figures 6(e) and 6(f) show the contour plots of $\Omega^{charge}_{xyy}(\omega, \omega, \boldsymbol{k})$ for monolayer $NbSe_2$ under light irradiation of $\hbar\omega = 1.5$ and 2.3 eV, respectively. In addition, below the each contour plot, the sliced $\Omega^{charge}_{xyy}(\omega, \omega, \boldsymbol{k})$ at $k_x = -\frac{\pi}{a}$, 0 and $\frac{\pi}{a}$ is shown. Here, blue, black, and red lines indicate $\Omega^{charge}_{xyy}(\omega, \omega\boldsymbol{k})$ at $k_x = -\frac{\pi}{a}$, 0 and $\frac{\pi}{a}$, respectively. $\Omega^{charge}_{xyy}(\omega, \omega, \boldsymbol{k})$ of $k_x = -\frac{\pi}{a}$ has opposite sign to that of $k_x = \frac{\pi}{a}$. Therefore, the k integration of $\Omega^{charge}_{xyy}(\omega, \omega, \boldsymbol{k})$ over the first BZ becomes identically zero, which is consistent with the result of Sec. III. Figures 6(g) and 6(h) show the contour plots of $\Omega^{charge}_{yxx}(\omega, \omega, \boldsymbol{k})$ in the first BZ under the light irradiation of $\hbar\omega = 1.5$ and 2.3 eV, respectively. Also, we show the sliced $\Omega^{charge}_{yxx}(\omega, \omega, \boldsymbol{k})$ at $k_x = -\frac{\pi}{a}$, 0, and $\frac{\pi}{a}$. Because $\Omega^{charge}_{yxx}(\omega, \omega, \boldsymbol{k})$ of $k_x = -\frac{\pi}{a}$ has the same sign to that of $k_x = \frac{\pi}{a}$, it is clear that the k integration of $\Omega^{charge}_{yxx}(\omega, \omega, \boldsymbol{k})$ over the first BZ becomes finite, which reproduces the result of Fig. 2(d). Thus, the nonlinear optical charge Hall current

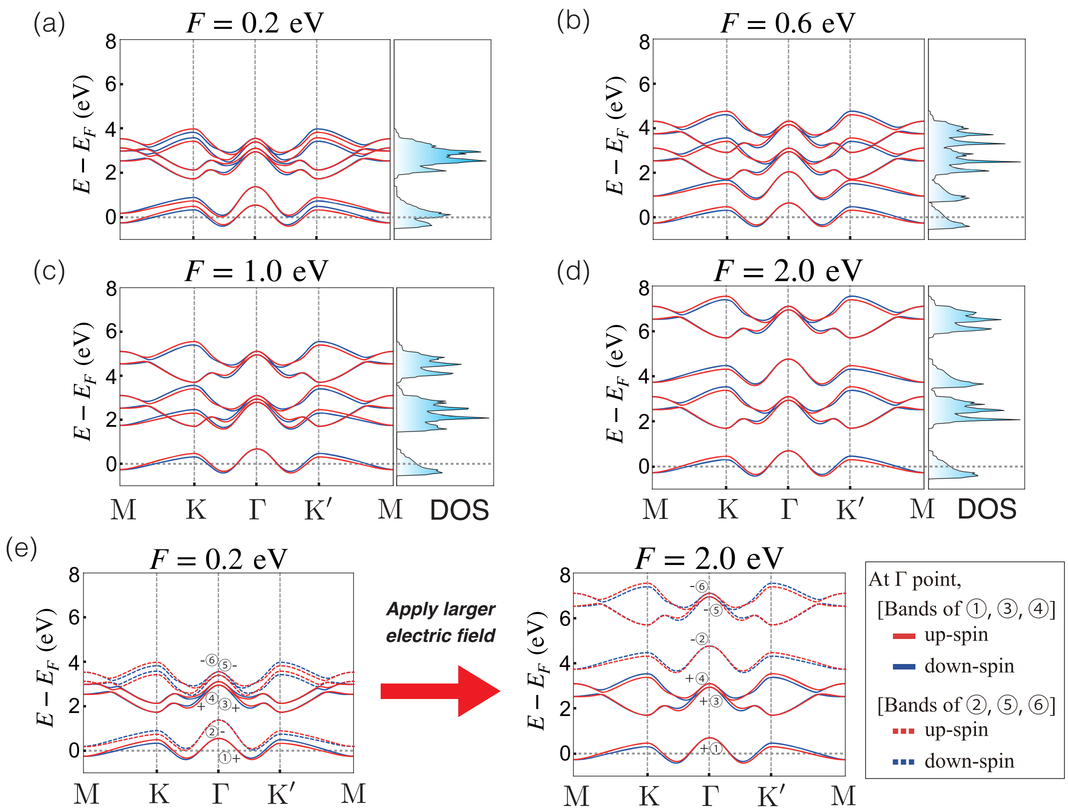

FIG. 7. Energy band structures of bilayer $NbSe_2$ with applied electric fields of (a) $F = 0.2$, (b) 0.6, (c) 1.0, and (d) 2.0 eV, respectively. Fermi levels are set to (a) −0.1370, (b) −0.5165, (c) −0.9113, and (d) −1.9074 eV, respectively. (e) Bilayer $NbSe_2$ with applied electric field includes six energy bands ① to ⑥. At Γ point, the energy bands of ①, ③, and ④ are shown by solid lines. The energy bands of ②, ⑤, and ⑥ are shown by dashed lines.

can be generated in y direction for monolayer $NbSe_2$ by irradiating x-polarized light.

APPENDIX D: ENERGY BAND STRUCTURES OF BILAYER $NbSe_2$ WITH APPLIED ELECTRIC FIELDS

Figures 7(a)–7(d) show the energy band structures and DOS of bilayer $NbSe_2$ for several different electric fields. Here, red and blue lines show spin-up and spin-down states, respectively. Owing to the broken inversion symmetry in bilayer $NbSe_2$ with applied electric fields, the energy band structures have larger spin splitting at the valence band edges in K and K' points the same as the case of odd-number-layered $NbSe_2$. In this paper we provide the energy band structures with applied electric fields of $F = 0.2$, 0.6, 1.0, and 2.0 eV, respectively. Fermi levels are set to −0.1370, −0.5165, −0.9113, and −1.9074 eV for the applied electric fields of $F = 0.2$, 0.6, 1.0, and 2.0 eV, respectively.

Figure 7(e) indicates the energy bands can move by applying larger electric field in bilayer $NbSe_2$. Here the energy

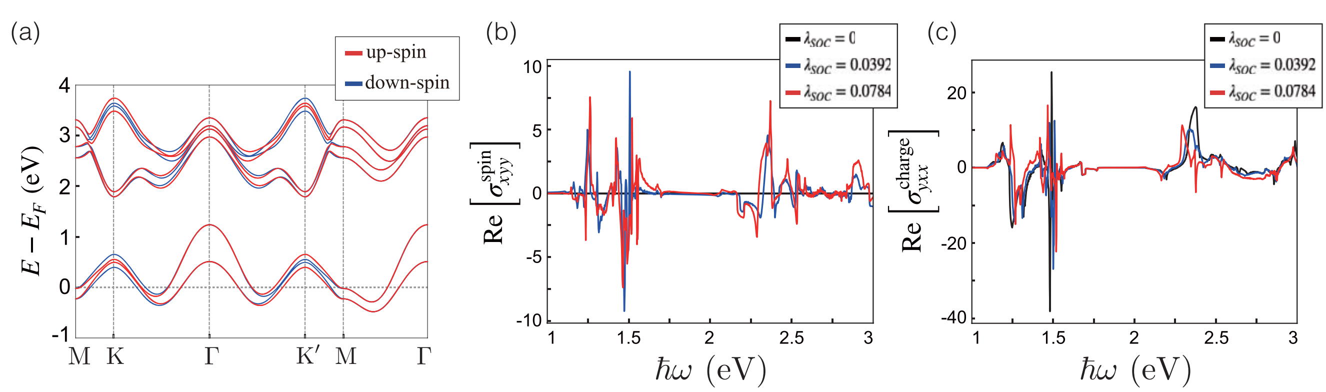

FIG. 8. (a) Energy band structure of bilayer $NbSe_2$ with each layer having a different Fermi energy. (b) Real part of nonlinear optical spin Hall conductivity $\mathrm{Re}[\sigma^{\mathrm{spin}}_{xyy}(\omega,\omega)]$ of decoupled bilayer $NbSe_2$. (c) Real part of nonlinear optical charge Hall conductivity $\mathrm{Re}[\sigma^{\mathrm{charge}}_{yxx}(\omega,\omega)]$ of decoupled bilayer $NbSe_2$. The units of $\mathrm{Re}[\sigma^{\mathrm{spin}}_{xyy}(\omega,\omega)]$ and $\mathrm{Re}[\sigma^{\mathrm{charge}}_{yxx}(\omega,\omega)]$ are e^2 and $e^3/\hbar$, respectively.

bands of solid lines (①, ③, and ④) have positive parity between upper and lower layers of bilayer $NbSe_2$, i.e., bonding molecular orbitals between the two layers. On the other hand, the energy bands of dashed lines (②, ⑤, and ⑥) have negative parity between layers, i.e., antibonding configuration. With an increase of electric field, the energy bands with negative (positive) parity shift up (down) to higher (lower) energy.

APPENDIX E: BILAYER $NbSe_2$ WITH EACH LAYER HAVING A DIFFERENT FERMI ENERGY

In this Appendix we consider the nonlinear optical spin and charge conductivities of bilayer $NbSe_2$ with each layer having a different Fermi energy, i.e., decoupled bilayer $NbSe_2$. Figure 8(a) shows the energy band structure of decoupled bilayer $NbSe_2$, where Fermi energy of the upper layer is $E_F = 0$ and that of the lower layer is 0.1 eV, respectively. Here, red and blue lines show spin-up and spin-down states, respectively. Since the upper and lower layers have the different Fermi energy, the energy band structure has spin splitting at K and K' points the same as the case of odd-number-layered $NbSe_2$.

Figures 8(b) and 8(c) show the real parts of nonlinear optical spin and charge Hall conductivities $\mathrm{Re}[\sigma^{\mathrm{spin}}_{xyy}(\omega,\omega)]$ and $\mathrm{Re}[\sigma^{\mathrm{charge}}_{yxx}(\omega,\omega)]$ of decoupled bilayer $NbSe_2$, respectively. Here both $\mathrm{Re}[\sigma^{\mathrm{spin}}_{xyy}(\omega,\omega)]$ and $\mathrm{Re}[\sigma^{\mathrm{charge}}_{yxx}(\omega,\omega)]$ are considered as the case of the SHG process and have Ising-type SOC parameter $\lambda_{\mathrm{SOC}} = 0.0784\,\mathrm{eV}$. Also, the cases for $\lambda_{\mathrm{SOC}} = 0.0392$ and 0 eV are plotted for the comparison. Because of the Fermi energy imbalance between upper and lower layers, the nonlinear optical spin and charge Hall conductivities become finite even in the bilayer $NbSe_2$, where several peaks appear below 1.5 and above 2.2 eV. The details of the imaginary parts of nonlinear optical spin and charge Hall conductivities are shown in the Supplemental Material [70].

[1] K. F. Mak, C. Lee, J. Hone, J. Shan, and T. F. Heinz, Atomically Thin MoS_2: A New Direct-Gap Semiconductor, Phys. Rev. Lett. **105**, 136805 (2010).

[2] A. Splendiani, L. Sun, Y. Zhang, T. Li, J. Kim, C.-Y. Chim, G. Galli, and F. Wang, Emerging photoluminescence in monolayer MoS_2, Nano Lett. **10**, 1271 (2010).

[3] S. Tongay, J. Zhou, C. Ataca, K. Lo, T. S. Matthews, J. Li, J. C. Grossman, and J. Wu, Thermally Driven crossover from indirect toward direct bandgap in 2D semiconductors: $MoSe_2$ versus MoS_2, Nano Lett. **12**, 5576 (2012).

[4] H. R. Gutiérrez, N. Perea-López, A. L. Elías, A. Berkdemir, B. Wang, R. Lv, F. López-Urías, V. H. Crespi, H. Terrones, and M. Terrones, Extraordinary room-temperature photoluminescence in triangular WS_2 monolayers, Nano Lett. **13**, 3447 (2013).

[5] W. Zhao, Z. Ghorannevis, L. Chu, M. Toh, C. Kloc, P.-H. Tan, and G. Eda, Evolution of electronic structure in atomically thin sheets of WS_2 and WSe_2, ACS Nano **7**, 791 (2013).

[6] A. Ciarrocchi, A. Avsar, D. Ovchinnikov, and A. Kis, Thickness-modulated metal-to-semiconductor transformation in a transition metal dichalcogenide, Nat. Commun. **9**, 919 (2018).

[7] M. Samadi, N. Sarikhani, M. Zirak, H. Zhang, H.-L. Zhang, and A. Z. Moshfegh, Group 6 transition metal dichalcogenide nanomaterials: Synthesis, applications and future perspectives, Nanoscale Horiz. **3**, 90 (2018).

[8] K. Thakar and S. Lodha, Optoelectronic and photonic devices based on transition metal dichalcogenides, Mater. Res. Express **7**, 014002 (2020).

[9] M. Wu, Y. Xiao, Y. Zeng, Y. Zhou, X. Zeng, L. Zhang, and W. Liao, Synthesis of two-dimensional transition metal dichalcogenides for electronics and optoelectronics, InfoMat **3**, 362 (2021).

[10] K. S. Novoselov, D. Jiang, F. Schedin, T. J. Booth, V. V. Khotkevich, S. V. Morozov, and A. K. Geim, Two-dimensional atomic crystals, Proc. Natl. Acad. Sci. U.S.A. **102**, 10451 (2005).

[11] S. B. Desai, S. R. Madhvapathy, M. Amani, D. Kiriya, M. Hettick, M. Tosun, Y. Zhou, M. Dubey, J. W. Ager III, D. Chrzan, and A. Javey, Gold-mediated exfoliation of ultralarge optoelectronically-perfect monolayers, Adv. Mater. **28**, 4053 (2016).

[12] Z. Lin, A. McCreary, N. Briggs, S. Subramanian, K. Zhang, Y. Sun, X. Li, N. J. Borys, H. Yuan, S. K. Fullerton-Shirey, A. Chernikov, H. Zhao, S. McDonnell, A. M. Lindenberg, K. Xiao, B. J. LeRoy, M. Drndic, J. C. M. Hwang, J. Park, M. Chhowalla *et al.*, 2D materials advances: From large scale synthesis and controlled heterostructures to improved characterization techniques, defects and applications, 2D Mater. **3**, 042001 (2016).

[13] J. Yu, X. Hu, H. Li, X. Zhou, and T. Zhai, Large-scale synthesis of 2D metal dichalcogenides, J. Mater. Chem. C **6**, 4627 (2018).

[14] S. Wang, J.-K. Huang, M. Li, A. Azam, X. Zu, L. Qiao, J. Yang, and S. Li, Growth of high-quality monolayer transition metal dichalcogenide nanocrystals by chemical vapor deposition and their photoluminescence and electrocatalytic properties, ACS Appl. Mater. Interfaces **13**, 47962 (2021).

[15] H. Zeng, J. Dai, W. Yao, D. Xiao, and X. Cui, Valley polarization in MoS_2 monolayers by optical pumping, Nat. Nanotechnol. **7**, 490 (2012).

[16] K. F. Mak, K. He, J. Shan, and T. F. Heinz, Control of valley polarization in monolayer MoS_2 by optical helicity, Nat. Nanotechnol. **7**, 494 (2012).

[17] T. Cao, G. Wang, W. Han, H. Ye, C. Zhu, J. Shi, Q. Niu, P. Tan, E. Wang, B. Liu, and J. Feng, Valley-selective circular dichroism of monolayer molybdenum disulphide, Nat. Commun. **3**, 887 (2012).

[18] H. Yu, X. Cui, X. Xu, and W. Yao, Valley excitons in two-dimensional semiconductors, Natl. Sci. Rev. **2**, 57 (2015).

[19] J. Sinova, S. O. Valenzuela, J. Wunderlich, C. H. Back, and T. Jungwirth, Spin Hall effects, Rev. Mod. Phys. **87**, 1213 (2015).

[20] P. N. Hai, Spin Hall effect in topological insulators, J. Magn. Soc. Jpn. **44**, 137 (2020).

[21] Y. K. Kato, R. C. Myers, A. C. Gossard, and D. D. Awschalom, Observation of the spin Hall effect in semiconductors, Science **306**, 1910 (2004).

[22] J. Wunderlich, B. Kaestner, J. Sinova, and T. Jungwirth, Experimental Observation of the Spin-Hall Effect in a Two-Dimensional Spin-Orbit Coupled Semiconductor System, Phys. Rev. Lett. **94**, 047204 (2005).

[23] X. Wen, Z. Gong, and D. Li, Nonlinear optics of two-dimensional transition metal dichalcogenides, InfoMat **1**, 317 (2019).

[24] L. Lafeta, A. Corradi, T. Zhang, E. Kahn, I. Bilgin, B. R. Carvalho, S. Kar, M. Terrones, and L. M. Malard, Second- and third-order optical susceptibilities across excitons states in 2D monolayer transition metal dichalcogenides, 2D Mater. **8**, 035010 (2021).

[25] A. Taghizadeh and T. G. Pedersen, Nonlinear optical selection rules of excitons in monolayer transition metal dichalcogenides, Phys. Rev. B **99**, 235433 (2019).

[26] M. L. Trolle, G. Seifert, and T. G. Pedersen, Theory of excitonic second-harmonic generation in monolayer MoS_2, Phys. Rev. B **89**, 235410 (2014).

[27] N. Kumar, S. Najmaei, Q. Cui, F. Ceballos, P. M. Ajayan, J. Lou, and H. Zhao, Second harmonic microscopy of monolayer mos_2, Phys. Rev. B **87**, 161403(R) (2013).

[28] D. J. Moss, J. E. Sipe, and H. M. van Driel, Empirical tight-binding calculation of dispersion in the second-order nonlinear optical constant for zinc-blende crystals, Phys. Rev. B **36**, 9708 (1987).

[29] E. Ghahramani, D. J. Moss, and J. E. Sipe, Full-band-structure calculation of second-harmonic generation in odd-period strained $(\mathrm{Si})_n/(\mathrm{Ge})_n$ superlattices, Phys. Rev. B **43**, 8990 (1991).

[30] L. M. Malard, T. V. Alencar, A. Paula M. Barboza, K. F. Mak, and A. M. de Paula, Observation of intense second harmonic generation from MoS_2 atomic crystals, Phys. Rev. B **87**, 201401(R) (2013).

[31] K. L. Seyler, J. R. Schaibley, P. Gong, P. Rivera, A. M. Jones, S. Wu, J. Yan, D. G. Mandrus, W. Yao, and X. Xu, Electrical control of second-harmonic generation in a WSe_2 monolayer transistor, Nat. Nanotechnol. **10**, 407 (2015).

[32] S. N. Rashkeev, W. R. L. Lambrecht, and B. Segall, Efficient *abinitio* method for the calculation of frequency-dependent second-order optical response in semiconductors, Phys. Rev. B **57**, 3905 (1998).

[33] S. N. Rashkeev and W. R. L. Lambrecht, Second-harmonic generation of I-III-VI_2 chalcopyrite semiconductors: Effects of chemical substitutions, Phys. Rev. B **63**, 165212 (2001).

[34] S. Sharma and C. Ambrosch-Draxl, Second-harmonic optical response from first principles, Phys. Scr. **T109**, 128 (2004).

[35] R. Leitsmann, W. G. Schmidt, P. H. Hahn, and F. Bechstedt, Second-harmonic polarizability including electron-hole attraction from band-structure theory, Phys. Rev. B **71**, 195209 (2005).

[36] Y. R. Shen, Surface properties probed by second-harmonic and sum-frequency generation, Nature (London) **337**, 519 (1989).

[37] Y. R. Shen, Revisiting the basic theory of sum-frequency generation, J. Chem. Phys. **153**, 180901 (2020).

[38] M. J. Shultz, C. Schnitzer, D. Simonelli, and S. Baldelli, Sum frequency generation spectroscopy of the aqueous interface: Ionic and soluble molecular solutions, Int. Rev. Phys. Chem. **19**, 123 (2000).

[39] G. L. Richmond, Molecular bonding and interactions at aqueous surfaces as probed by vibrational sum frequency spectroscopy, Chem. Rev. **102**, 2693 (2002).

[40] Y. R. Shen and V. Ostroverkhov, Sum-frequency vibrational spectroscopy on water interfaces: Polar orientation of water molecules at interfaces, Chem. Rev. **106**, 1140 (2006).

[41] S. Gopalakrishnan, D. Liu, H. C. Allen, M. Kuo, and M. J. Shultz, Vibrational spectroscopic studies of aqueous interfaces: Salts, acids, bases, and nanodrops, Chem. Rev. **106**, 1155 (2006).

[42] T. Ishiyama, T. Imamura, and A. Morita, Theoretical studies of structures and vibrational sum frequency generation spectra at aqueous interfaces, Chem. Rev. **114**, 8447 (2014).

[43] T. Y. F. Tsang, Optical third-harmonic generation at interfaces, Phys. Rev. A **52**, 4116 (1995).

[44] J. A. Squier, M. Müller, G. J. Brakenhoff, and K. R. Wilson, Third harmonic generation microscopy, Opt. Express **3**, 315 (1998).

[45] C. Stock, K. Zlatanov, and T. Halfmann, Third harmonic generation and microscopy, enhanced by a bias harmonic field, Opt. Commun. **457**, 124660 (2020).

[46] B. Dromey, M. Zepf, A. Gopal, K. Lancaster, M. S. Wei, K. Krushelnick, M. Tatarakis, N. Vakakis, S. Moustaizis, R. Kodama, M. Tampo, C. Stoeckl, R. Clarke, H. Habara, D. Neely, S. Karsch, and P. Norreys, High harmonic generation in the relativistic limit, Nat. Phys. **2**, 456 (2006).

[47] C. Winterfeldt, C. Spielmann, and G. Gerber, Colloquium: Optimal control of high-harmonic generation, Rev. Mod. Phys. **80**, 117 (2008).

[48] G. Vampa, C. R. McDonald, G. Orlando, D. D. Klug, P. B. Corkum, and T. Brabec, Theoretical Analysis of High-Harmonic Generation in Solids, Phys. Rev. Lett. **113**, 073901 (2014).

[49] M. Pawlicki, H. A. Collins, R. G. Denning, and H. L. Anderson, Two-photon absorption and the design of two-photon dyes, Angew. Chem., Int. Ed. **48**, 3244 (2009).

[50] M. Rumi and J. W. Perry, Two-photon absorption: an overview of measurements and principles, Adv. Opt. Photon. **2**, 451 (2010).

[51] G. Wang, D. Bennett, C. (John) Zhang, C. Ó Coileáin, M. Liang, N. McEvoy, J. J. Wang, J. Wang, K. Wang, V. Nicolosi, and W. J. Blau, Two-photon absorption in monolayer MXenes, Adv. Opt. Mater. **8**, 1902021 (2020).

[52] T. K. Fryett, A. Zhan, and A. Majumdar, Phase-matched nonlinear optics via patterning layered materials, Opt. Lett. **42**, 3586 (2017).

[53] J. He, D. Wei, and X. Wang, Quasi-phase matching for a nonlinear photonic waveguide enabled by monolayer transition-metal dichalcogenide arrays, J. Korean Phys. Soc. **79**, 380 (2021).

[54] R.-C. Xiao, D.-F. Shao, Z.-Q. Zhang, and H. Jiang, Two-Dimensional Metals for Piezoelectriclike Devices Based on Berry-Curvature Dipole, Phys. Rev. Appl. **13**, 044014 (2020).

[55] B. T. Zhou, C.-P. Zhang, and K. T. Law, Highly Tunable Nonlinear Hall Effects Induced by Spin-Orbit Couplings in Strained Polar Transition-Metal Dichalcogenides, Phys. Rev. Appl. **13**, 024053 (2020).

[56] Q. Ma, S.-Y. Xu, H. Shen, D. MacNeill, V. Fatemi, T.-R. Chang, A. M. M. Valdivia, S. Wu, Z. Du, C.-H. Hsu, S. Fang, Q. D. Gibson, K. Watanabe, T. Taniguchi, R. J. Cava, E. Kaxiras, H.-Z. Lu, H. Lin, L. Fu, N. Gedik *et al.*, Observation of the nonlinear Hall effect under time-reversal-symmetric conditions, Nature (London) **565**, 337 (2019).

[57] I. Sodemann and L. Fu, Quantum Nonlinear Hall Effect Induced by Berry Curvature Dipole in Time-Reversal Invariant Materials, Phys. Rev. Lett. **115**, 216806 (2015).
[58] J. A. Wilson, F. J. Di Salvo, and S. Mahajan, Charge-density waves and superlattices in the metallic layered transition metal dichalcogenides, Adv. Phys. **50**, 1171 (2001).
[59] S. Kim and Y.-W. Son, Quasiparticle energy bands and Fermi surfaces of monolayer $NbSe_2$, Phys. Rev. B **96**, 155439 (2017).
[60] W.-Y. He, B. T. Zhou, J. J. He, N. F. Q. Yuan, T. Zhang, and K. T. Law, Magnetic field driven nodal topological superconductivity in monolayer transition metal dichalcogenides, Commun. Phys. **1**, 40 (2018).
[61] X. Xi, Z. Wang, W. Zhao, J.-H. Park, K. T. Law, H. Berger, L. Forró, J. Shan, and K. F. Mak, Ising pairing in superconducting $NbSe_2$ atomic layers, Nat. Phys. **12**, 139 (2016).
[62] E. Sohn, X. Xi, W.-Y. He, S. Jiang, Z. Wang, K. Kang, J.-H. Park, H. Berger, L. Forró, K. T. Law, J. Shan, and K. F. Mak, An unusual continuous paramagnetic-limited superconducting phase transition in 2D $NbSe_2$, Nat. Mater. **17**, 504 (2018).
[63] A. Anikin, R. D. Schaller, G. P. Wiederrecht, E. R. Margine, I. I. Mazin, and G. Karapetrov, Ultrafast dynamics in the high-symmetry and in the charge density wave phase of $2H$-$NbSe_2$, Phys. Rev. B **102**, 205139 (2020).
[64] C.-S. Lian, C. Si, J. Wu, and W. Duan, First-principles study of Na-intercalated bilayer $NbSe_2$: Suppressed charge-density wave and strain-enhanced superconductivity, Phys. Rev. B **96**, 235426 (2017).
[65] J. M. Lu, O. Zheliuk, I. Leermakers, N. F. Q. Yuan, U. Zeitler, K. T. Law, and J. T. Ye, Evidence for two-dimensional Ising superconductivity in gated MoS_2, Science **350**, 1353 (2015).
[66] Y. Saito, Y. Nakamura, M. S. Bahramy, Y. Kohama, J. Ye, Y. Kasahara, Y. Nakagawa, M. Onga, M. Tokunaga, T. Nojima, Y. Yanase, and Y. Iwasa, Superconductivity protected by spin-valley locking in ion-gated MoS_2, Nat. Phys. **12**, 144 (2016).
[67] B. T. Zhou, N. F. Q. Yuan, H.-L. Jiang, and K. T. Law, Ising superconductivity and Majorana fermions in transition-metal dichalcogenides, Phys. Rev. B **93**, 180501(R) (2016).
[68] L. Bawden, S. P. Cooil, F. Mazzola, J. M. Riley, L. J. Collins-McIntyre, V. Sunko, K. W. B. Hunvik, M. Leandersson, C. M. Polley, T. Balasubramanian, T. K. Kim, M. Hoesch, J. W. Wells, G. Balakrishnan, M. S. Bahramy, and P. D. C. King, Spin-valley locking in the normal state of a transition-metal dichalcogenide superconductor, Nat. Commun. **7**, 11711 (2016).
[69] R. Habara and K. Wakabayashi, Optically induced spin current in monolayer $NbSe_2$, Phys. Rev. B **103**, L161410 (2021).
[70] See the Supplemental Material at http://link.aps.org/supplemental/10.1103/PhysRevResearch.4.013219 for nonlinear optical Hall conductivity of the SFG process. Temperature effect and behavior of TMDC semiconductor on nonlinear optical spin and charge Hall currents are also presented.
[71] G.-B. Liu, W.-Y. Shan, Y. Yao, W. Yao, and D. Xiao, Three-band tight-binding model for monolayers of group-VIB transition metal dichalcogenides, Phys. Rev. B **88**, 085433 (2013).
[72] N. L. Kang and S. D. Choi, Derivation of nonlinear optical conductivity by using a reduction identity and a state-dependent projection method, J. Phys. A: Math. Theor. **43**, 165203 (2010).
[73] H. J. Lee, N. L. Kang, J. Y. Sug, and S. D. Choi, Calculation of the nonlinear optical conductivity by a quantum-statistical method, Phys. Rev. B **65**, 195113 (2002).
[74] N. L. Kang and S. D. Choi, Derivation of second-order nonlinear optical conductivity by the projection-diagram method, AIP Adv. **2**, 012161 (2012).
[75] N. L. Kang, S.-S. Lee, and S. D. Choi, Projection-reduction method applied to deriving non-linear optical conductivity for an electron-impurity system, AIP Adv. **3**, 072104 (2013).
[76] C. Aversa and J. E. Sipe, Nonlinear optical susceptibilities of semiconductors: Results with a length-gauge analysis, Phys. Rev. B **52**, 14636 (1995).
[77] J. E. Sipe and E. Ghahramani, Nonlinear optical response of semiconductors in the independent-particle approximation, Phys. Rev. B **48**, 11705 (1993).
[78] Q. Y. Lu, N. Bandyopadhyay, S. Slivken, Y. Bai, and M. Razeghi, Room temperature single-mode terahertz sources based on intracavity difference-frequency generation in quantum cascade lasers, Appl. Phys. Lett. **99**, 131106 (2011).
[79] A. Ruehl, A. Gambetta, I. Hartl, M. E. Fermann, K. S. E. Eikema, and M. Marangoni, Widely-tunable mid-infrared frequency comb source based on difference frequency generation, Opt. Lett. **37**, 2232 (2012).
[80] D. J. Passos, G. B. Ventura, J. M. B. Lopes dos Santos, and J. M. Viana Parente Lopes, Nonlinear optical conductivity of a two-band crystal I, J. Phys.: Condens. Matter **33**, 465701 (2021).
[81] C. Zeng, S. Nandy, and S. Tewari, Nonlinear transport in Weyl semimetals induced by Berry curvature dipole, Phys. Rev. B **103**, 245119 (2021).
[82] S. Kim and Y.-W. Son, Dichotomy of saddle points in energy bands of monolayer $NbSe_2$, Phys. Rev. B **104**, 045426 (2021).